日本磁気学会
ISSN 2432-0250
Journal of the Magnetics Society of Japan
Electronic Journal URL: https://www.jstage.jst.go.jp/browse/msjmag

Vol.48 No.6　2024

Journal

Physics of Magnetism, Utilization of High Magnetic Fields

Thin Films, Fine Particles, Multilayers, Superlattices

Spintronics

Biomagnetism / Medical Applications

JOURNAL OF THE MAGNETICS SOCIETY OF JAPAN

Vol.48 No.6 2024

日本磁気学会

ISSN 2432-0250

HP: http://www.magnetics.jp/ e-mail: msj@bj.wakwak.com
Electronic Journal: http://www.jstage.jst.go.jp/browse/msjmag

Journal of the Magnetics Society of Japan
Vol. 48, No. 6

Electronic Journal URL: https://www.jstage.jst.go.jp/browse/msjmag

CONTENTS

Physics of Magnetism, Utilization of High Magnetic Fields

Thin Films, Fine Particles, Multilayers, Superlattices

Spintronics

Biomagnetism / Medical Applications

J. Magn. Soc. Jpn., **48**, 94-107 (2024) <Paper>

Comparative study of electronic structure in ferromagnetic Heusler alloys Ni_2MnX (X = Al, Ga, In) using the quasi-particle self-consistent *GW* method

J. Luštinec*, **, M. Obata*, R. Majumder*, K. Hyodo*, T. Kotani***, L. Kalvoda**, and T. Oda*
* Division of Mathematical and Physical Sciences, Graduate School of Natural Science and Technology, Kanazawa Uni., *Kakuma machi, Kanazawa 920-1192, Japan*
** Department of Solid State Engineering, Faculty of Nuclear Science and Engineering, Czech Technical Uni. in Prague, *Břehová 7, Prague 1, 115 19, Czech Republic*
*** Advanced Mechanical and Electronic System Research Center, Department of Engineering, Tottori Uni., *Tottori, 680-8552, Japan*

A comparative study of cubic Heusler alloys Ni_2MnX (X = Al, Ga, In) was performed to explain the differences in material properties using a first-principles electronic structure calculation of quasi-particle self-consistent *GW* (QSGW) method. The obtained electronic structures indicate a similar density of states (DOS) of Ni $3d$ e_g orbitals on the Fermi level for all the studied materials, implying a promotion to a band Jahn-Teller (BJT) distortion. The generalized susceptibility analysis suggests some instability of the cubic high symmetry phase and indicates, that the Ga containing material is the one which is the most pronounced to 10M modulation due to this instability. Taking the advantage of accurate first-principles electronic structure calculations performed by QSGW, the U parameters of Hubbard correction on Mn and Ni atoms were determined using the density functional theory (DFT) approach with generalized gradient approximation (GGA), so that the local and total QSGW magnetic moments are reproduced.

Keywords: martensite transformation, Heusler alloys, magnetic shape memory, generalized susceptibility, QSGW, Fermi surface

1. Introduction

Since discovery of magnetic shape memory (MSM) effect in Ni–Mn–Ga[1], ferromagnetic Heusler alloys have been considered as the most promising MSM material. The MSM effect consists of two separate phenomena: the magnetically induced martensite transformation (MIM), and the magnetically induced reorientation of martensite (MIR) occuring when the magneto-stress is large enough to overcome the twinning stress[2]. The MSM effect belongs to so-called multi-ferroic phenomena since ferromagnetism and ferroelasticity are coupled in MIR due to the magnetocrystalline anisotropy, resulting in a great interest in MSM.

The MSM effect was reported in ferromagnetic, antiferromagnetic and even in paramagnetic materials. Thus, ferromagnetism is not always necessary for the MSM effect (details are, for example, in the review paper[3]). Furthermore, the iron-based alloys of Fe–Pd and Fe–Pt also exhibit the MSM effect[4]. Nevertheless, Ni–Mn–Ga based alloys are still the most promising magnetic shape memory materials. Countless experimental and theoretical studies have been performed to explain this giant MSM effect in Ni–Mn–Ga, including other possible contributing mechanisms, such as the influence of exact composition and doping. The substitution of Ga atoms with chemically similar atoms, e.g. Al or In, has also been studied as these materials are promising candidates for the MSM effect. To some extent, Ni–Mn–Al and Ni–Mn–In indicated an MSM effect in specific situations, e.g., after annealing of the samples. In this work, electronic structures of three Heusler alloys, Ni_2MnX with X = Al, Ga, In, are theoretically investigated using a state-of-the-art approach of first-principles calculation. A quasi-particle self-consistent *GW* (QSGW) method[5] is applied to explain differences among the material properties, since a more proper and precise description of electron localization effects is required compared to the description included in the standard density functional theory (DFT) calculations[6]. Using QSGW, the cubic phase of Ni_2MnGa indicates a modulation vector coinciding with the experimental one, suggesting a formation of the experimentally observed modulated phase[7]. This discovery is a breakthrough in the history of theoretical studies for Ni–Mn–Ga systems. Thus, the magnetic metallic materials should be theoretically reinvestigated based on such advanced levels of electronic structure calculations. This work aims to provide one of these contributions.

The high-temperature structure of Ni–Mn–Ga is an $L2_1$ Heusler structure (space group no. 225 $Fm\bar{3}m$). With the decreasing temperature, a phase transition to martensite occurs, resulting in several martensite phases with different structures. Non-modulated martensite (NM) with the $L1_0$ structure was considered the ground state of Ni–Mn–Ga[2]. Additionally, several modulated phases exist with either commensurate or incommensurate modulation: six-layered (6M)

Corresponding author: J. Luštinec (e-mail: lustijak@cvut.cz).

INDEX

premartensite[8], five-layered (10M; stacking sequence $(32)^2$) modulation[9], and seven-layered (14M; stacking sequence $(52)^2$) modulation[9]. The modulation wave vector evolves with temperature[10] and also under mechanical stress[11]. Further, DFT calculations predicted an orthorhombic four-layered structure (4O) to be the most stable modulated structure[12], but the 4O has never been observed experimentally for Ni–Mn–Ga. Recently, the GGA+U method, which includes additional Hubbard U corrections to DFT GGA calculation, provided a reasonable agreement between the calculations and the experimental observations that 10M is the ground state of Ni–Mn–Ga[6]. The MSM effect is observed only for samples containing 10M and 14M phases, implying the importance of modulated phases (and of the modulation at all) for the MSM effect to occur. Magnetically induced stress in Ni–Mn–Ga can reach up to 11% for 14M and 6% for 10M[3].

Ni–Mn–Al alloys crystallize in three main structures: a high-temperature partially-ordered cubic B2 structure (CsCl–type), a fully-ordered cubic $L2_1$ structure, and a low-symmetry $L1_0$ tetragonal structure. (One can refer to the descriptions, e.g., in the articles[13,14].) The positions of Mn and Al atoms are interchangeable in the B2 structure, resulting in complicated exchange interactions. The ordering temperature of B2 to $L2_1$ transition is relatively low in Ni–Mn–Al compared to Ni–Mn–Ga. The specific composition of these phases in a sample of austenite significantly influences the magnetic properties of Ni–Mn–Al[15]. The B2 structure is antiferromagnetic, but the $L2_1$ structure is ferromagnetic. The crystal structure of Ni–Mn–Al depends on the composition and the history of heat treatment of the samples. For instance, the quenched samples show the B2 structure, while the slowly cooled ones include a mixture of the $L2_1$ and the B2 structures[16]. The $L1_0$ martensite phase appears in the low-Al and low-Mn content alloys[17] and has never been observed for stoichiometric Ni_2MnAl, as also confirmed by first-principles calculations[15,18-20]. Furthermore, the modulated martensite structures (such as 10M, 12M with the stacking sequence 5232, and 14M) can be created in alloys with low-Al and high–Mn content (a phase diagram shown in[13]). Reversible deformation in Ni–Mn–Al reaches from 0.4% to 0.7% with 1000 thermal cycles[14]. However, this deformation is significantly lower compared to the deformations observed in Ni–Mn–Ga, reaching 6% for 10M and 11% for 14M modulations.

Ni–Mn–In austenite crystallizes in a fully-ordered $L2_1$ structure with ferromagnetic ordering[21]. The stoichiometric composition, whose Curie temperature is 314 K [22], does not indicate a martensite transformation at low temperatures, as Ni_2MnAl[19,23]. However, the martensite transformation occurs in off-stoichiometric compositions of low-In and high-Mn[24,25]. The magnetic properties of Ni–Mn–In are similar to those in Ni–Mn–Ga[26]: Curie temperatures, occurrences of ferromagnetism and paramagnetism in the phase diagram along the non-stoichiometric composition. The similarity is further apparent with the effect of substituting Mn atoms with Ni for X = In and X = Ga[21,27]. The NM occurred for a significantly off-stoichiometric composition of $Ni_{0.50}Mn_{0.45}In_{0.05}$[25]. Additionally, 10M, 14M, and 4O modulated structures have been reported in low-In and high-Mn samples[24,25]. The 4O was in coexistence with other martensite phases for the $Ni_{0.50}Mn_{0.35}In_{0.15}$ sample[24]. The influence of the compound composition on the tetragonal distortion was shown by Liu et al.[28]. The increase of Mn atoms and decrease of In atoms concentrations result in different dependence of the c/a ratio on the total energy stabilizing either the modulated or the non-modulated martensite.

The formation of modulated phases in Ni–Mn–Ga for a specific composition range begins with the creation of premartensite associated with a phonon softening of a transversal acoustic TA_2 mode in [110] direction, with the wave vector $\mathbf{q} = 2\pi/a\ [\xi\xi 0]$, $\xi = 0.33$[29]. The generalized susceptibility $\chi(\mathbf{q})$ can give insight into the phonon softening that indicates the instability of austenite. First, the generalized susceptibility of Ni_2MnGa was studied by Velikokhatnyi and Naumov[30] using DFT with local spin-density approximation (LDA), resulting in an observation of the nesting wave vector parameter $\xi \approx 0.42$. The authors concluded that the formation of the 10M phase is preferable rather than the premartensite. However, the quantitative value of ξ was not definitively related to the formation of 10M or premartensite. Later, Lee et al.[31] studied the generalized susceptibility with the Stoner approximation to include temperature dependence by changing the magnetization, revealing the Fermi surface nesting vector dependence on the magnetization. Using GGA instead of LDA resulted in better agreement between experimental and theoretical results[23,32]. To further decrease the differences, the Hubbard U parameter was added to the DFT calculations, as performed by Zelený et al. [6]. As a result, they obtained an appropriate sequence of the total energies among the martensite phases in concern with the experimental results. Bagutlin et al.[33] used the strongly constrained and appropriately normed (SCAN) meta-GGA functional (hereafter refer as SCAN) containing the self-interaction corrections (SIC). Using this approach and SCAN–U (negative U approach), the authors performed a parametric study along the measure of SIC in both the Fermi surface nesting vector, and the magnetic moment. For a full SIC configuration (SCAN–U with $U = 0$), they reported the nesting wave vectors, $\xi_1 = 0.23$ and $\xi_2 = 0.78$ (see Fig. 4. in Ref.[33]), with a relatively large magnetic moment $M_{tot} = 4.73\ \mu_B/\mathrm{f.u.}$. The authors suggest that the SCAN functional behaves as a GGA+U approach with $U \approx 2$ eV, resulting in modifications of the Fermi surface. Recently, the QSGW method was applied for the electronic structure calculations of Ni_2MnGa to evaluate the disagreement with the published DFT results, indicating that the two Fermi surface nesting vectors are $\xi_1 = 0.20$ and $\xi_2 =$

0.78, respectively[7)]. The authors claimed that, for the first time, the former ξ_1 obtained by QSGW corresponds well corresponds to the experimentally observed modulation of the martensite phase for the stoichiometric composition of Ni_2MnGa (10M). QSGW total magnetic moment was increased compared to experimental measurements, specifically $M_{tot} = 4.74\ \mu_B/\mathrm{f.u.}$. Interestingly, these values of ξ_1, ξ_2 and M_{tot} are similar to those obtained by the SCAN[33)]. Recently, the Hubbard parameter *U* for Ni atoms was applied and investigated, resulting in a conclusion that U_{Ni}, such as 3–5 eV, provides a set of material properties comparable to experimental results, including the magnetic moments and others, for both the austenite and NM martensite in Ni_2MnGa[34)].

The electronic structures obtained by the QSGW method for the following Heusler alloys, Ni_2MnX (X = Al, Ga, In), are reported in this work. Further, the GGA+U method with a new approach for choosing the *U* parameters was applied to provide similar results as QSGW. The electronic instabilities of these materials were investigated caused by the Fermi surface nesting using the generalized susceptibility. Subsequently, other electronic structure properties were analyzed and compared with experimental observations and other theoretical methods. In conclusion, the profile of generalized susceptibility for X = Ga was the sharpest among the three studied materials.

2. Methods and computational details

Electronic structures and their properties were investigated employing the quasi-particle self-consistent *GW* method[5),35)-37)]. For comparison, we also have used conventional methods of density functional theory with generalized gradient approximation[38)] and with additional Hubbard *U* corrections[39)]. All of these methods were implemented in the ecalj package[40)], which utilizes an all-electron mixed basis. This package has contributed to providing a lot of achievements on magnetic metal, as described in the Introduction. The eigenvalues and eigenfunctions $\{\epsilon_i, \Psi_i(\mathbf{r})\}$, where i is a combined index of band index n, spin index σ, and $\mathbf{k}$-point: $i = (n\sigma\mathbf{k})$, are obtained from the following one-particle Hamiltonian:

$$[-\hbar^2/[2m]\nabla^2 + V_{\mathrm{ext}} + V_{\mathrm{H}} + V_{\mathrm{XC}}]|\Psi_i\rangle = \epsilon_i|\Psi_i\rangle, \qquad (1)$$

where V_{ext} , V_{H} and V_{XC} are nuclei, Hartree, and exchange-correlation potentials, respectively. Once an appropriate V_{XC} is obtained, the eigenvalues and eigenfunctions may be determined in a self-consistent loop procedure (DFT loop), as in a usual DFT calculation. In the QSGW method, another self-consistent loop (*GW* loop) is employed to determine V_{XC};

$$V_{\mathrm{XC}} = 1/2\, \Sigma_{ij}|\Psi_i\rangle\{\mathrm{Re}[\Sigma(\epsilon_i)]_{ij} + \mathrm{Re}[\Sigma(\epsilon_j)]_{ij}\}\langle\Psi_j|, \qquad (2)$$

where Re and $\Sigma(\epsilon_i)$ represents the Hermitian part and the self-energy, respectively. The latter $\Sigma(\epsilon_i)$ is determined by *GW* approximation: $\Sigma = iGW$ (this *i* means the imaginary unit), where *G* and *W* are the Green's function made of eigenvalues and eigenfunctions, and the screened Coulomb interaction, respectively. The latter is determined using the random phase approximation: $W = (1 - v\Pi)^{-1}v$, where the polarization function (Π) and the bare Coulomb interaction (v). After new V_{XC} is determined from the *GW* loop, new $\{\epsilon_i, \Psi_i(\mathbf{r})\}$ can be obtained from the DFT loop. These loops were repeated until the convergence condition was satisfied: the change of quasi-particle energy eigenvalues is less than 1 meV for all of the orbitals, spin, and k-points $i = (n\sigma\mathbf{k})$.

The advantage of QSGW is to provide a better mean-field potential based on the *GW* self-energy, as suggested in Eq. (2), compared to DFT (LDA or GGA). Such QSGW potential typically gives not only the contribution of correcting band gaps and effective mass for semiconductors, but also the contribution like Hubbard *U*. These improvements are consequences of two types of contributions sought to the originals of off-site and on-site in the screened Coulomb interaction[41)]. As a result, the energy position of *d*-orbitals with the anion level is modified according to the on-site effect, and the band width narrows due to the off-site one.

All the studied systems in this work are full-Heusler intermetallic compounds with a general formula X_2YZ and its Strukturbericht designation of full-Heusler structure is $L2_1$ with symmetry of a cubic space group Fm $\bar{3}$ m (No. 225). The $L2_1$ structure and the corresponding 1st. Brillouin zone (BZ) is shown in Fig. 1. The lattice constants used in the theoretical calculations are experimentally measured ones for the stoichiometric intermetallic compounds Ni_2MnX (X = Al, Ga, In), as listed in Table 1. We note that, since the QSGW currently does not allow us to access the total internal energy, we cannot determine the equilibrium lattice constant as the minimum of total internal energy.

Electronic susceptibility is sometimes used for a response to atomic displacements. The properties of such susceptibility originate from both the matrix elements of electron-phonon interaction (EPI) and Fermi surface nesting (FSN) in the materials. They contribute to a set of long range atomic forces so that one discusses modulation at the occurrence of structural phase transition. Details of theoretical procedure can be referred to a standard approach[44)]. Although the matrix elements of EPI can contribute to a discussion of material properties, the present work has been focused on the behaviors of FSN as a first step to investigate a possibility of phase transition to occur. When neglecting the wave vector dependence in the EPI, the intrinsic part of susceptibility (generalized susceptibility) is presented as

$$\chi(\mathbf{q}) = \frac{1}{N_{\mathbf{k}}}\sum_{n,n',\boldsymbol{k},\sigma}\frac{f(\epsilon^{\sigma}_{n\mathbf{k}+\mathbf{q}}) - f(\epsilon^{\sigma}_{n'\mathbf{k}})}{\epsilon^{\sigma}_{n'\mathbf{k}} - \epsilon^{\sigma}_{n\mathbf{k}+\mathbf{q}}}, \qquad (3)$$

where $N_{\mathbf{k}}$ is the number of $\mathbf{k}$-points in the 1st BZ and $\epsilon^{\sigma}_{n\mathbf{k}}$ and $f(\epsilon^{\sigma}_{n\mathbf{k}})$ are the eigenvalue and Fermi-Dirac distribution function, respectively, for the states $(n\sigma\mathbf{k})$.

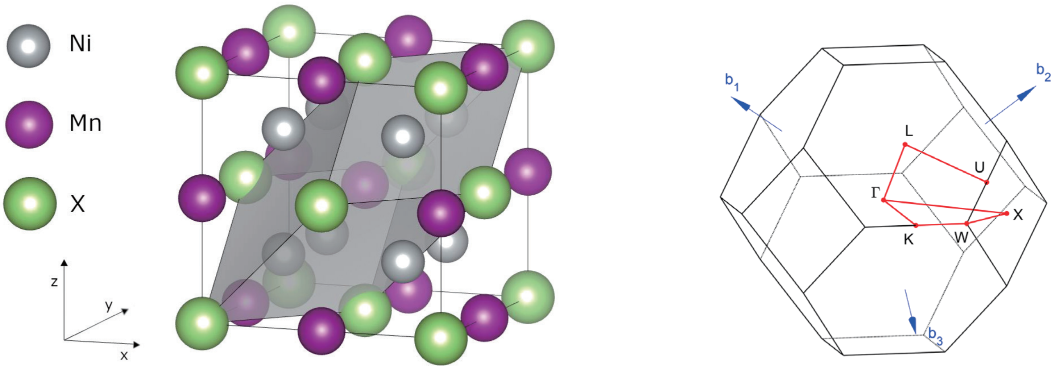

(a) (b)

Fig. 1 (a) Conventional and primitive (grey) cells of FCC lattice for studied compounds and (b) Brillouin zone of FCC lattice with symmetry points and paths.

Table 1 Lattice constants of the full-Heusler $L2_1$ structures for Ni_2MnX (X = Al, Ga, In) used in the calculations.

	Ni_2MnAl	Ni_2MnGa	Ni_2MnIn
lattice constant [Å]	5.882[a]	5.825[b]	6.078[c]

[a] Ref.[42], [b] Ref.[43], [c] Ref.[21]

This $\chi(\mathbf{q})$ has a large value when the condition of FSN is satisfied: one of the levels $\epsilon^{\sigma}_{n'\mathbf{k}}$ and $\epsilon^{\sigma}_{n\mathbf{k}+\mathbf{q}}$ is exclusively occupied giving $\epsilon^{\sigma}_{n'\mathbf{k}} \sim \epsilon^{\sigma}_{n\mathbf{k}+\mathbf{q}}$. The system instability may occur with the fluctuating modulation specified by wave vector $\mathbf{q}$ if the value of $\chi(\mathbf{q})$ is large for this wave vector $\mathbf{q}$. The analysis of the rigid band model can be applied to the investigation of $\chi(\mathbf{q})$[7]. In this work, we focused on the investigation with total magnetic moment changes. This is because the previous work found that the tracing of magnetic moment (magnetic rigid band model) may efficiently reproduces a picture of modulation properties to the chemical composition between Mn and Ga elements. Such a reproduction of the chemical composition corresponds to the increase of Mn composition ($Ni_2Mn_{1+x}Ga_{1-x}$) and contributes to the increase of magnetization rather than a simple increase in the number of electrons. These pictures of electron occupation are consistent with the results of the previous supercell calculation[45] for some extent of composition, where the ferromagnetic state is favorable.

In the present work, $\chi(\mathbf{q})$ is calculated at the grid points of 192×192×192 in the cubic Brillouin zone. In the GGA calculations, Perdew-Burke-Ernzerhof[38] (PBE) exchange and correlation functional is utilized with the grid points of 16×16×16 for the DFT loop. For the *GW* loop, the grid points of 8×8×8 are employed for the self-energy calculation.

In addition to the investigations by QSGW, this work employed a novel approach for GGA+U. To improve the description of *d*-states at the transition metals, Hubbard correction *U* can be applied in DFT calculations. In the previous works on Ni_2MnGa[34),46], such correction on Ni as well as on Mn atoms was already suggested as one of the ways to improve the theoretical description by the GGA+U method. Using such an approach, an agreement or disagreement of results can be discussed based on comparing the calculated quantities with those obtained by GGA or QSGW methods. As a new approach, the *U* parameters are fitted for each compound in this work so that the calculated atomic and total magnetic moments are in accordance with the QSGW values.

3. Results

3.1 Magnetic moments

The total and atomic magnetic moments of QSGW tend to be increased compared to those of GGA in ferromagnetic systems[47]. As shown in Fig. 2 and Table 2, all these values of QSGW become larger by about 16% than the corresponding GGA values at the total moment. On atomic moments, although the Mn atomic moment increased by only a few %, the Ni atomic moment became much larger by about 65%. These tendencies were similar to those described in the previous work by the SCAN for Ni_2MnGa[33]. The total magnetic moment of QSGW has a value almost the same as that of the SCAN (4.726 μ_B/f.u.). Note that the latter was obtained at the theoretical equilibrium lattice constant shorter by 1.7% than the presently-used experimental one.

Unfortunately, QSGW magnetic moments are significantly larger compared to the experimental values. In speculation to the theoretical viewpoints on the first-principles, further advanced methods should provide magnetic moments closer to the experimental value. Including spin fluctuations into the random phase approximation used in QSGW may partially solve this issue[48].

Among the three materials of X = Al, Ga and In, the X = In case has relatively large magnetic moments, especially the Mn atomic moments are increased by 0.3 μ_B. Comparing the other two materials, i.e., X = Al and Ga, the magnetic moments are slightly suppressed for X = Ga. This tendency is observed for GGA, as shown in

Table 2 Total magnetic moments [μ_B/f. u.] and atomic magnetic moments [μ_B/atom] in Ni_2MnX (X = Al, Ga, In), calculated with GGA, QSGW, and GGA+U approaches. Experimental values are included for comparison.

	Method, U_{Mn} [eV], U_{Ni} [eV]	Magnetic moments [μ_B]			
		Ni	Mn	X	Total
Ni_2MnAl	GGA	0.397	3.467	-0.058	4.203
	QSGW	0.649	3.604	-0.045	4.857
	GGA+U, U_{Mn} : 0, U_{Ni} : 4.5	0.657	3.591	-0.059	4.846
	GGA+U, U_{Mn} : 0.1, U_{Ni} : 4.5	0.652	3.611	-0.060	4.855
	GGA+U, U_{Mn} : 0.2, U_{Ni} : 4.25	0.637	3.627	-0.061	4.840
	experiment[a]				4.19
Ni_2MnGa	GGA	0.365	3.429	-0.047	4.112
	QSGW	0.605	3.558	-0.035	4.733
	GGA+U, U_{Mn} : 0.1, U_{Ni} : 4.75	0.602	3.586	-0.045	4.745
	experiment[b]				4.17
Ni_2MnIn	GGA	0.345	3.657	-0.045	4.302
	QSGW	0.577	3.884	-0.035	5.003
	GGA+U, U_{Mn} : 0.5, U_{Ni} : 5.0	0.577	3.889	-0.047	4.996
	experiment[c]				4.29

[a] Ref.[42], [b] Ref.[43], [c] Ref.[21]

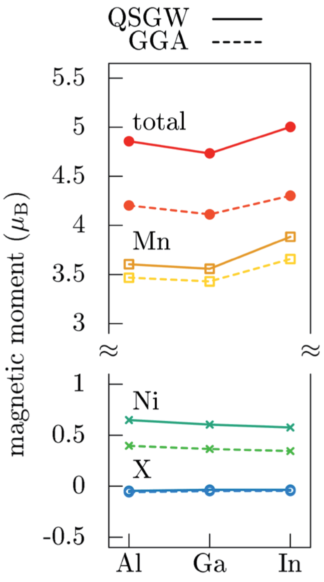

Fig. 2 Magnetic moments of studied systems Ni_2MnX (X = Al, Ga, In) calculated by QSGW (full lines) and GGA (broken lines), where red, yellow, green, and blue lines are the total, Mn atomic, Ni atomic, and X atomic magnetic moments, respectively.

Table 2. The Mn component of the wavefunction may be relatively delocalized, according to the discussion of electron localization.

The magnetic moments of GGA are almost similar to those in the previous works with GGA[19),21),33)]. For example, the total moments of GGA are comparable to the published values: 4.07, 4.23, and 4.20 μ_B for X = Al[19)], Ga[19)], and In[21)], respectively. The magnetic moments slightly deviate depending on the selected method of electronic structure calculation and the details of computational settings. The discussions related to the results of GGA+U will appear in the later subsections.

3.2 Effective *U* parameters

the GGA+U successfully reproduce those obtained by QSGW. For all studied compounds, the *U* on Mn atom (U_{Mn}) is significantly smaller than the recommended value of 1.8 eV which provided the total energy sequence among the several martensites of Ni_2MnGa consistent with the experimental observations[6)]. The *U* on Ni atom (U_{Ni}) tends to be large because the Ni atomic magnetic moment of QSGW becomes enlarged by about two-thirds compared to the GGA value. The fitted results are in the following: U_{Mn} = 0.1 eV and U_{Ni} = 4.75 eV for Ni_2MnGa, U_{Mn} = 0.5 eV and U_{Ni} = 5.0 eV for Ni_2MnIn. For Ni_2MnAl, the three sets of *U*s provided the similar results: U_{Mn} = 0, 0.1, 0.2 eV with U_{Ni} = 4.5, 4.5, 4.25 eV, respectively. The initial guess was done based on the previously published works by Zelený et al.[6)] and Janovec et al.[34)]. The total and local magnetic moment dependence on the choice of Hubbard *U* parameters on Ni and Mn atoms is in Fig. 3. The U_{Mn} has effect only on Mn atoms, but U_{Ni} increases the local magnetic moments on both Mn and Ni atoms for all studied materials.

As described before, the obtained parameter U_{Mn} is smaller than those typically presented in the previous works of the tetragonal system[6)], while the U_{Ni} is relatively larger. This fact means that there is a

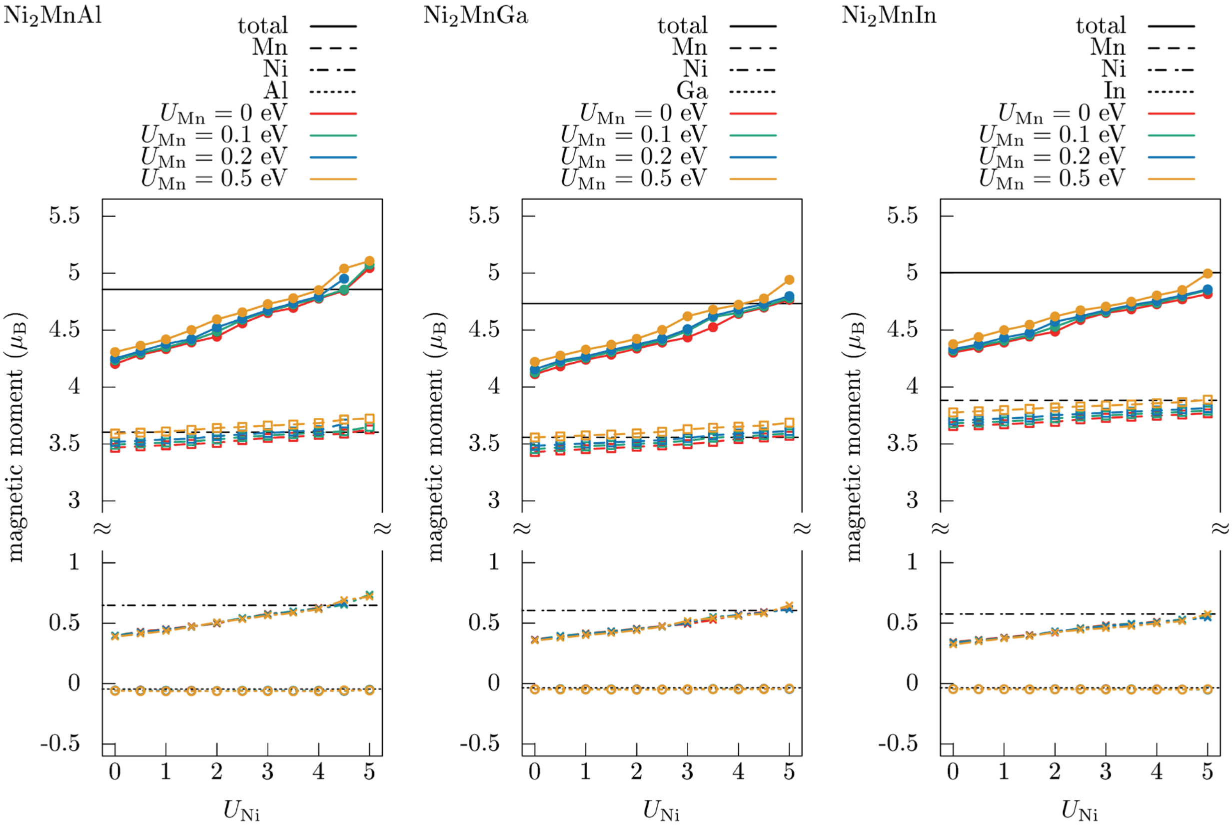

Fig. 3 Dependence of total and local magnetic moments on the choice of Hubbard U parameters on Mn and Ni atoms for studied compounds Ni_2MnX (X = Al, Ga, In). The horizontal black lines correspond to the total and local magnetic moments obtained by the QSGW method. Filled circles indicate total magnetic moment, squares local magnetic moment on Mn atoms, crosses local magnetic moment on Ni atoms, and empty circles local magnetic moments on X atoms (Al, Ga, In).

difference between Mn and Ni atoms on the realistic electron localization effect in the GGA approach. We will discuss the electronic structures obtained for GGA+U in the later subsection 4.1.

3.3 Total density of states

The total density of states (DOS) is presented for the three studied cases: X = Al, Ga and In, in Fig. 4. The exchange splitting observed between the majority and minority spin states is larger in QSGW compared with GGA, as reflected in an enhancement of total magnetic moment. In QSGW, the DOS's peak, which may relate to a band Jahn-Teller (BJT) effect, is located just at the Fermi level, while in the GGA case, the peak is shifted by 0.2 eV below the Fermi level. This discrepancy is a consequence of the GGA drawbacks removed in the advanced method. The peak of the BJT effect has a component of Ni e_g orbitals. This component may split into occupied and unoccupied levels in the martensite phases of local tetragonal symmetry. Since U_{Mn} and U_{Ni} are obtained in the new way, the GGA+U approach reproduced the total and atomic magnetic moments of QSGW, as shown in Table 2, implying that the exchange splitting of the total DOS is similar between the QSGW and GGA+U. In the total DOS of GGA+U, the energy position of BJT's peak coincides with that of QSGW. As shown in Fig. 4, however, the large body of occupied DOS is lowered in energy by about 1 eV, compared with those of GGA or QSGW. Further analysis of this behavior in the case of GGA+U follows in the later subsection 4.1.

3.4 Partial density of states

Figure 5 shows the projected components of the Mn and Ni d-orbitals. The e_g and t_{2g} components of the occupied (majority spin) states are clearly separated on the Mn atom, while these kinds of separation are negligible for the unoccupied (minority spin) state. On the Mn atom, the exchange splitting between the two parts for t_{2g} extends to 3 ~ 3.5 eV. On the Ni atom, the exchange splitting is significantly less dispersive than on Mn. Further, the separation between e_g and t_{2g} is more apparent, especially for the minority spin state. One of the separated peaks lies just on the Fermi level and mainly consists of the e_g component, confirming the descriptions at Fig. 4 (see the previous subsection).

Comparing these PDOSs with those of GGA (top and bottom frames in Fig. 5), though the trend of PDOS is similar, the width of each peak shape becomes narrower

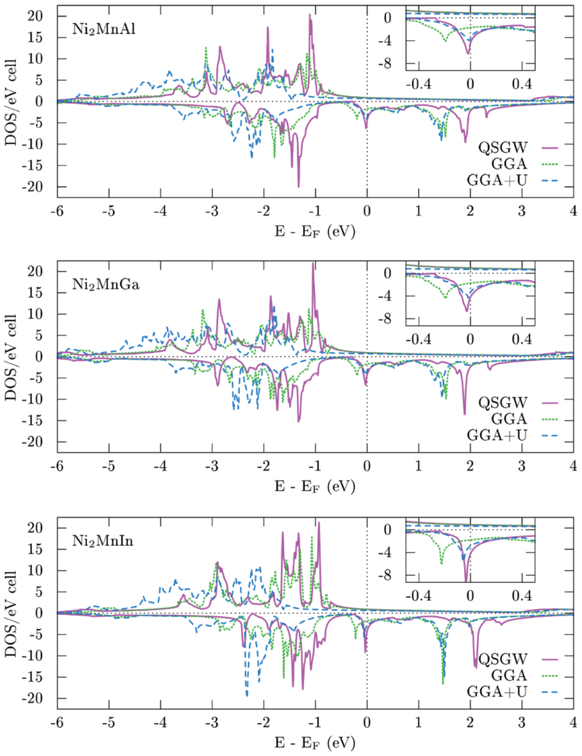

Fig. 4 Total density of states: QSGW and GGA+U compared with GGA for (top), X=Al, (middle) X=Ga, and (bottom figure) X=In. Positive DOS values are for majority-spin state and the negative for minority-spin state.

for the QSGW method, as a consequence of the electron localization effect in the *d*-orbitals. Moreover, the position of the BJT peak and the width of exchange splitting decreases for all the three materials in the case of GGA. However, these slight differences observed in the PDOS might not provide insight into the different experimental behavior among the three studied materials.

3.5 Band dispersion curves

As shown in Fig. 6, for Ni$_2$MnAl and Ni$_2$MnGa, two minority spin bands cross the Fermi level: in the case of Ni$_2$MnIn, there are three such bands. The differences among Ni$_2$MnX (X = Al, Ga, In) at Γ point are also apparent: The energy levels corresponding to the Mn 3*d*-orbitals states (minority spin t_{2g} on the Fermi level in Ni$_2$MnGa) are shifted above the Fermi level for Ni$_2$MnIn compared to the Ni$_2$MnGa, causing the increase of magnetic moment on the Mn atom for Ni$_2$MnIn (see the figures of magnetic moments and DOS given in Fig. 2 and 5).

In Fig. 6, at the Fermi level, the band width is approximately 0.2 ~ 0.3 eV along a Γ point to another Γ one, indicating a clear flat band. These flat bands appear in all the three materials and are assigned to the origin of the BJT peak in the DOS (Fig. 4 and Fig. 5). Existence of the flat bands can provide an instability of electronic states. As reported for the case of X = Ga[7], the calculated

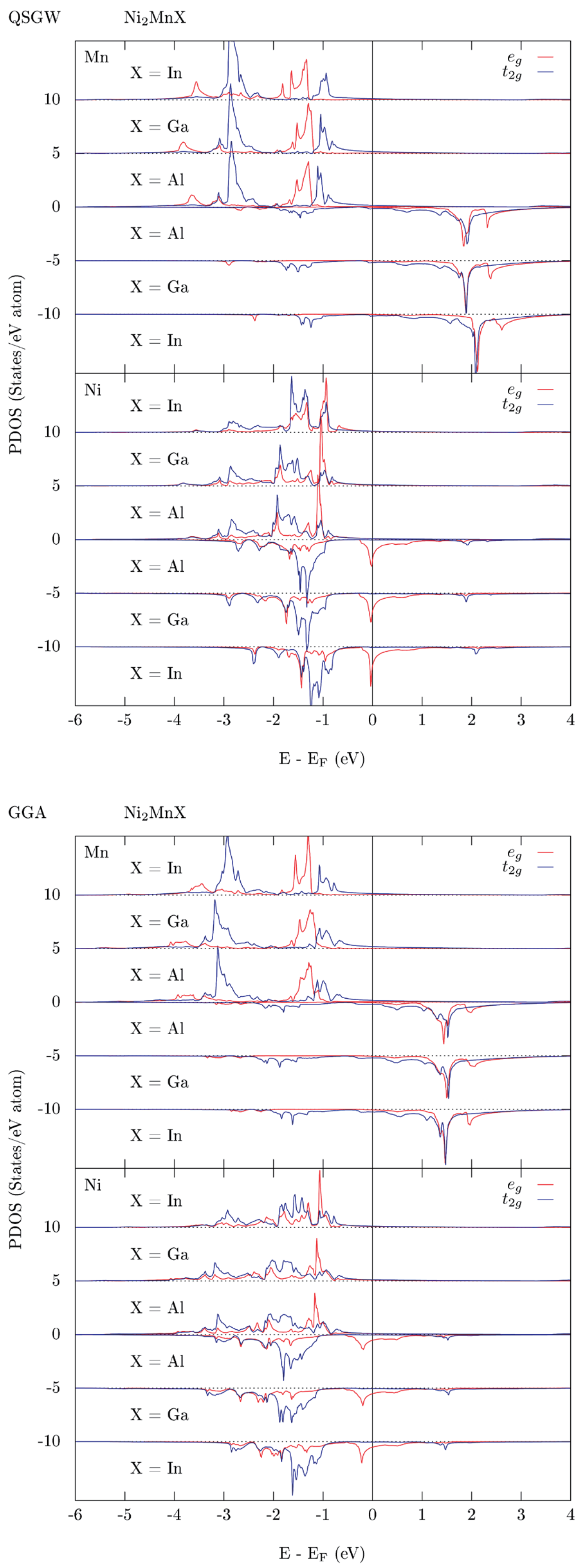

Fig. 5 Comparison of partial density of states (PDOS) of QSGW and GGA projected to the *d*-orbitals (t_{2g} and e_g) on Ni and Mn atoms among Ni$_2$MnX (X=Al, Ga, In). Positive PDOS values are for majority-spin state and the negative for minority-spin state.

FSN vector coincided with a modulation vector obtained by the experimental measurement. Among the materials of Ni_2MnX, the electronic structures are similar around the Fermi level. Thus, the properties of FSN are also necessary to compare.

3.6 Generalized susceptibility

The wave vector of FSN for X = Ga has been reported as $\xi = 0.2$ in the previous work7). In this work, we compare profiles of the generalized susceptibility presented by Eq. (3) among the materials of X = Al, Ga and In. In Fig. 7, the comparison of reduced generalized $\chi(\mathbf{q})/\chi(0)$ is presented as a contour map of the xy-plane with $q_z = 0$. A sharp peak is observed around $2\pi/a$ (0.2, 0.2, 0) in all three materials. The peak position slightly shifts to a shorter wave vector for X = Al and a longer one for X = In. However, the peak is the sharpest for X = Ga along the direction [110], as shown in Fig. 8. The peak shapes are broadened for X = Al and X = In compared to the case of X = Ga.

The figures of Fermi surfaces also provide insight into the observed peak positions. Figure 9 indicates the flat cuts of Fermi surfaces at $k_z = 0$, $2\pi/a \times 0.25$, and $2\pi/a \times 0.5$. The three-dimensional Fermi surfaces are summarized in the Appendix. These square-like curves convince us to intuitively understand the peak formation around $2\pi/a$ (0.2, 0.2, 0) position. The Fermi surfaces for the three materials are similar, but the subtle differences are apparent in Fig. 9.

The broad profiles of $\chi(\mathbf{q})$ for X = Al and X = In imply that the sensitivity of expected phase transitions becomes suppressed or smeared. Indeed, any experimental observation of phase transition to 10M modulated phases has never been reported for stoichiometric cases of X = Al and X = In. In an off-stoichiometric composition of X = Al (low compositions of Al and high composition of Mn in $Ni_2Mn_{1-x}Al_x$), the 10M modulated phases have been observed13). According to that experimental work, the phase boundary between 10M and B2 (paramagnetic) phases along the Al composition can be extrapolated to near the stoichiometric composition at low temperatures, but the B2 (antiferromagnetic) phase was reported to appear around such composition. The reduced $\chi(\mathbf{q})$ calculated with GGA is given for the better comparison among the three materials in Fig. 8(b). The profiles of $\chi(\mathbf{q})$ for X = Al and X = In calculated by GGA are similar to those of X = Ga. As suggested in the previous work7), the profile obtained by GGA does not give sufficient features for the discussions related to the experimental observations.

Detailed analysis of the generalized susceptibility with **q** in [110] direction is performed for studied compounds. As suggested in the previous theoretical works on X = Ga29)-31), the generalized susceptibility has a couple of nesting vectors (peaks) at ξ_1 (small) and ξ_2 (large) as $2\pi/a\,(\xi\xi0)$. The property of such peaks appears commonly in the results. The nesting vector parameters are $\xi_1 = 0.208$ and $\xi_2 = 0.771$ for Ni_2MnGa (Fig. 8(a)).

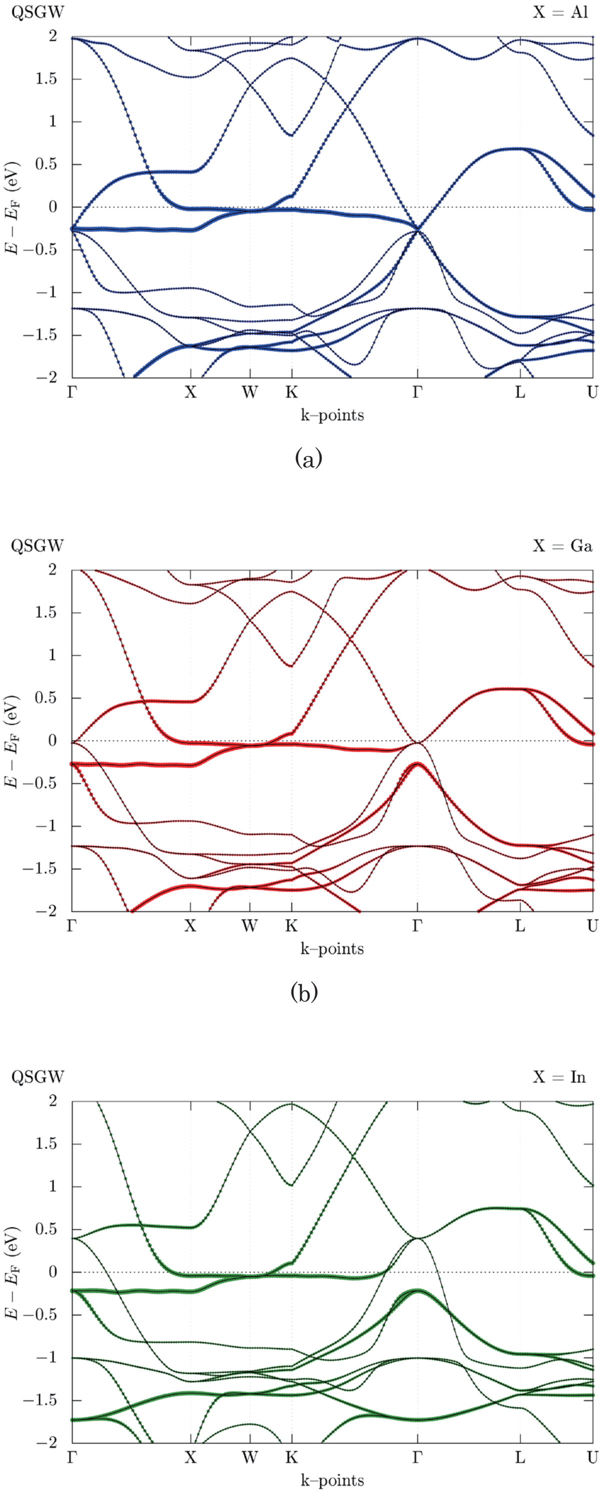

(a)

(b)

(c)

Fig. 6 Comparison of the band dispersion curves of QSGW for the minority-spin state among (a) Ni_2MnAl, (b) Ni_2MnGa, and (c) Ni_2MnIn. The enhanced color indications show a size of projected components for Ni e_g orbital.

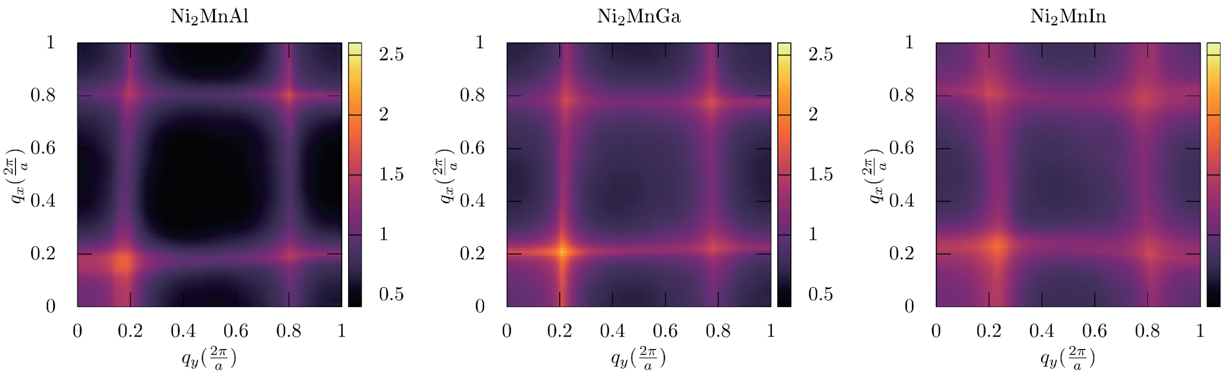

Fig. 7 Comparison of the contour map in *xy*-plane for the reduced generalized susceptibilities of QSGW among Ni_2MnX (X = Al, Ga, In).

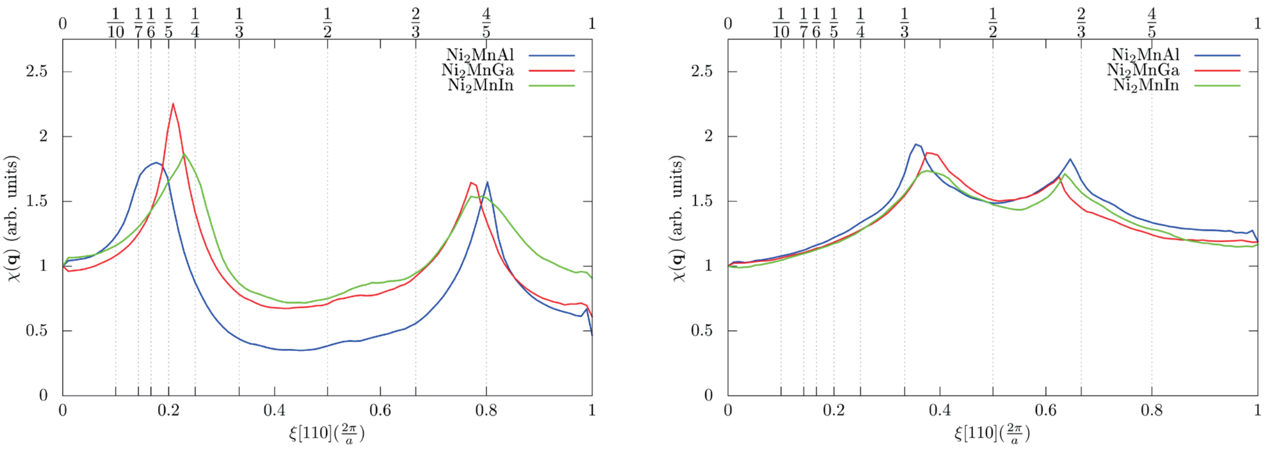

(a) (b)

Fig. 8 Comparison of the generalized susceptibility along the [110] direction among the studied compounds calculated by (a) QSGW and (b) GGA.

These numbers are similar to those obtained by the SCAN (ξ_1 = 0.23 and ξ_2 = 0.78 reported in Fig. 4(c) in Ref.[33])).

For Ni_2MnAl, the nesting vector ξ_1 is 0.177, which is comparable to 1/6 (corresponding to the 12M modulation observed for off-stoichiometric Ni–Mn–Al[13])) if the magnetic rigid band model with the change of magnetization +0.02 μ_B is applied. However, this peak is blunt, as pointed out before (see Fig. 8(a)) for the case without any change of magnetization as well as for the increased magnetization (using rigid band model) by +0.02 μ_B (Fig. 10(a)), implying a possible coexistence of 10M, 14M, and 12M phases. This phase coexistence appears at room temperature for 17 < x < 19 in $Ni_{50}Mn_{50-x}Al_x$[13]). The issue is that the experimental results for stoichiometric composition and samples with only fully ordered $L2_1$ structure have not been successfully created, causing difficulties in making any conclusion.

Applying the rigid band model for the change of magnetization (magnetic rigid band model) may be viewed as a simulation of chemical composition change. The FSN vector parameters are modified when the magnetization of the system is changed. Lowering the magnetization results in decreasing the difference between ξ_1 and ξ_2, i.e. the peaks get closer to each other, and the peaks overlap in the case of GGA calculations (the magnetization dependence is not shown) for the −0.48 μ_B change of magnetization in Ni_2MnAl and N Ni_2MnIn with values being almost 1/2. For Ni_2MnGa, the overlap is incomplete, and a further decrease in magnetization would be needed. The decrease in magnetization generally leads to decrease of the peak separation ($|\xi_1 - \xi_2|$) and to decrease of the peak value in $\chi(\mathbf{q})/\chi(0)$ (see Fig 10).

On the other hand, an increase in the total magnetization generally results in increasing both the separation of the nesting vector peaks and corresponding peak values. For Ni_2MnGa, the shift of ξ_1 from 1/5 (10M) to 1/7 (14M) is observed with the increased total magnetization by 0.12 or 0.14 μ_B in QSGW calculations[7]. The FSN vector parameters are ξ_1 = 1/3 and ξ_2 = 2/3, indicating the 6M premartensite[29] if the total magnetic moment is reduced by −0.40 μ_B for Ni–Mn–Ga in the

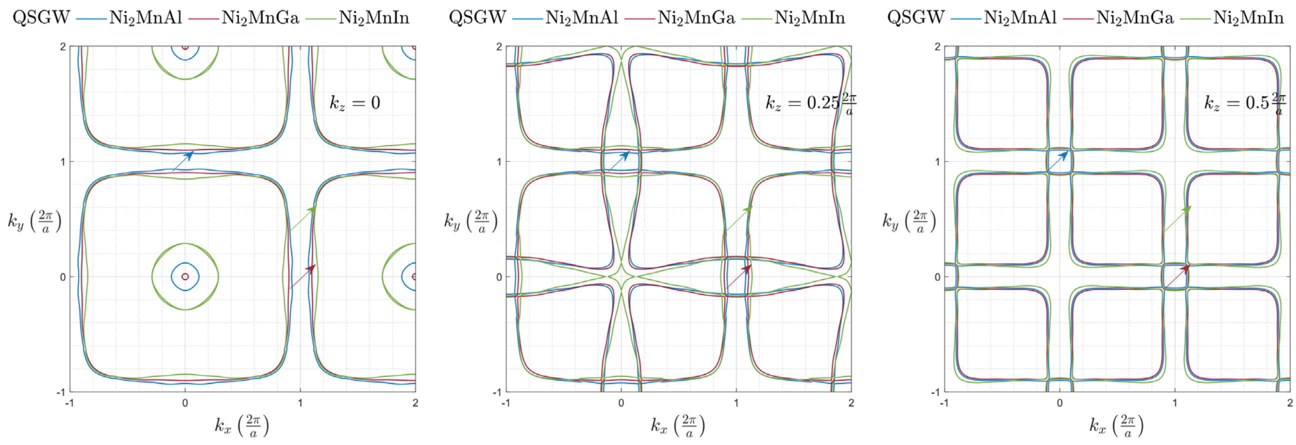

(a) (b) (c)

Fig. 9 Comparison on the intersecting curves of Fermi surfaces calculated by QSGW in the planes (a) $k_z = 0$, (b) $k_z = 2\pi/a \times 0.25$ and (c) $k_z = 2\pi/a \times 0.5$.

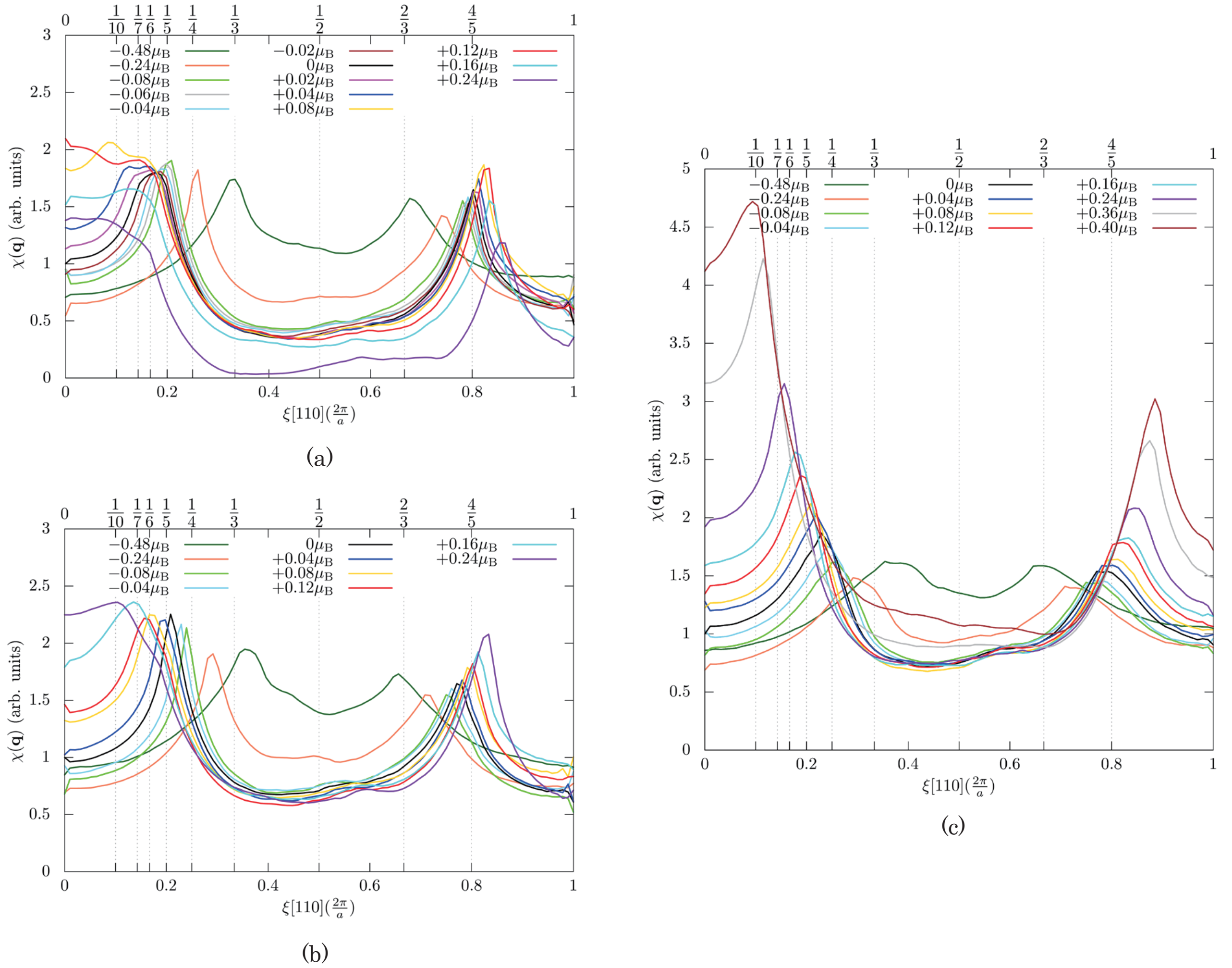

(a) (b) (c)

Fig. 10 Generalized susceptibilities of the magnetic rigid band model for (a) Ni$_2$MnAl, (b) Ni$_2$MnGa and (c) Ni$_2$MnIn. Note that the change of magnetization is μ_B per formula units (f.u.).

case of QSGW. This observation implies that the premartensite occurs with a lowering temperature from austenite and, further decreasing of the temperature (an increase of the magnetization) results in the creation of the modulated structures such as 10M and 14M. For Ni$_2$MnAl, the generalized susceptibility peak, which is blunt at the self-consistent case, sharps for the FSN vector parameter ξ_1 while decreasing the magnetization of the system. The maxima ξ_1 is sharp for the system with the lowered magnetization by 0.08 μ_B, at ξ_1 = 1/5.

The values of ξ_1 = 1/3 and ξ_2 = 2/3 for −0.48 μ_B indicate the creation of the premartensite as in Ni_2MnGa. The peaks suggesting the premartensite are present for Ni_2MnIn as well, but the peak shapes are blunter than the other two compounds. In the case of Ni_2MnIn, if the magnetization is increased by +0.08 μ_B, the FSN parameter ξ_1 is 0.208, corresponding to the instability to the 10M phase. With further increasing of magnetization, the 14M phase should appear for the increase of magnetization over +0.24 μ_B. The maximal value of the generalized susceptibility is reached when the change of magnetization is +0.40 μ_B where the FSN vector parameter ξ_1 is 0.1. On the other hand, the modulated structures for Ni–Mn–In are observed for the high-Mn and low-In contents.

4. Discussions

4.1 Verification of GGA+U

The introduction of Hubbard +U scheme with the first-principles DFT[39] has been used to partially eliminate defects of DFT approaches: lack of electron localization effect, over-binding on condensation, and others. Although the U parameter can be determined in a self-consistent way in the scheme or by reproducing an appropriate physical quantity and comparing with corresponding experimental values, in this work, the GGA+U was introduced and evaluated for reproducing the QSGW's data of magnetic moments. As presented in the subsection 3.2, the U parameters successfully reproduce these magnetic moments. In Fig. 4 and Fig. 11, the total DOS and PDOS are reported for GGA+U. For X=Al, the third set of parameters (U_{Mn} : 0.2 eV, U_{Ni} : 4.25 eV) was used for drawing the figures as representative.

The DOS obtained by GGA+U indicates a BJT peak at the Fermi level for the minority spin. The energy position of the peak is well reproduced compared with those of QSGW for the three materials. Unfortunately, there are several differences between the GGA+U and QSGW, involving namely the widths and energy positions for the d-orbitals of Mn and Ni at the occupied and unoccupied states far from the Fermi energy. The energy positions of occupied states can be measured by the photoelectron spectroscopy (PES). Indeed, the peaks in the PES profile have been observed around the energy positions of 0.3 eV and 1.5 eV near the Fermi energy in stoichiometric Ni_2MnGa[49]. The position of the peak around 0.3 eV is shifted depending on the sample composition[50]. Concerned about the formal peak position, the peak around 1.5 eV is well described by both QSGW and GGA. However, the peak closer to the Fermi level (0.3 eV) is shifted to the Fermi level in QSGW, and thus, the agreement between theory and experiment became worse in QSGW than in GGA. The cause of the observed QSGW behavior requires further investigation in the future.

Figure 12 shows the generalized susceptibilities calculated with GGA+U for X = Al, Ga and In. As shown in the figure, the profiles are not similar to those of QSGW (Fig. 8). For X = Ga, the instability towards a lower symmetry, i.e., the tetragonal one, represented by the modulation wave vector $2\pi/a$ [110], may not be manifested based on the calculated profile of the generalized susceptibility. For X = Al, the profile also becomes broader. For X = In, as a result, the profile of GGA+U is obtained as similar to that of QSGW.

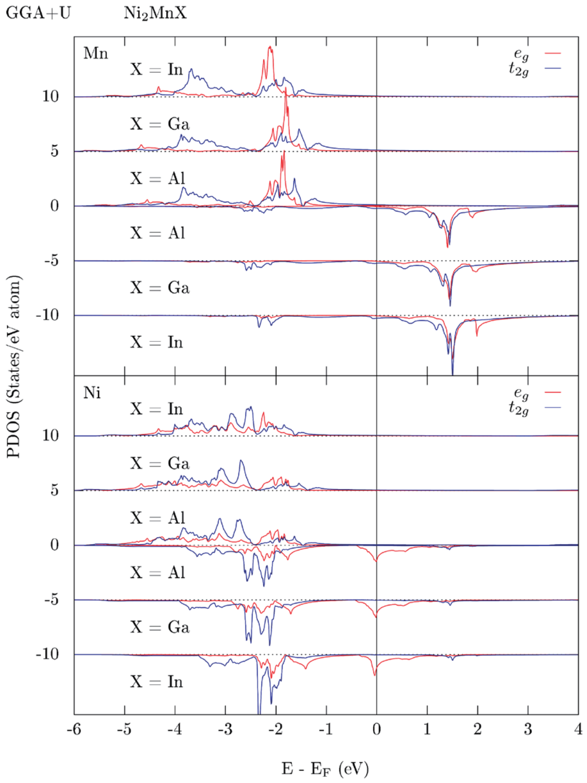

Fig. 11 Partial density of states of GGA+U projected to the d-orbitals (t_{2g} and e_g) in Ni_2MnX (X=Al, Ga, In). Positive PDOS values are for majority-spin state and the negative for minority-spin state.

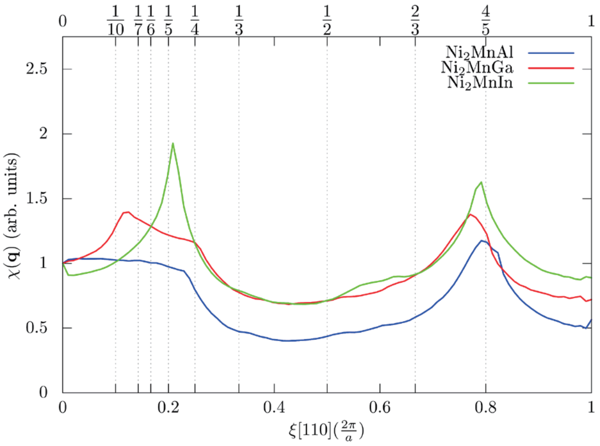

Fig. 12 Generalized susceptibility of Ni_2MnX (X=Al, Ga, In) calculated with GGA+U method.

Using the GGA+U method, the results of generalized susceptibility indicate more similarities with QSGW results. However, the peak position depends on the specific choice of the Hubbard U parameters for the systems. Based on the Hubbard U parameters in this work (4.5 – 5 eV for Ni atoms and 0 – 0.5 eV for Mn atoms), the importance of the additional localization of the Ni d-states is revealed for the proper description of the electronic structures in the studied Heusler compounds.

4.2 Connection to experimental results

By the first-principles approach of QSGW, the trend among the three materials indicates that the most intense possible instability to modulation along the direction [110] is predicted for X = Ga, as is pointed out in Fig. 7. In the results of experimental measurements, the phase transition to the martensite phase of 10M has been observed for X = Ga, while such kind of phase transition has never appeared on the stoichiometric composition for X = Al and X = In. Focusing on off-stoichiometric compositions, which may be discussed based on the theoretical approach of the magnetic rigid band model, an instability of 14M modulation can be preferable for X = Ga, as discussed in the previous report of QSGW7).

For X = In and Al, no martensite phase has been experimentally observed at the stoichiometric composition. However, for off-stoichiometric compositions, several martensite phases have been already reported for a long history of related Heusler alloys. Here, the chemical compositions of Mn-rich or Ni-rich materials are discussed: $Ni_2Mn_{1+x}X_{1-x}$, $Ni_{2+y}Mn_{1-y}X$. In the case of X = In, the 10M modulated structure25,51) occurred for the Mn-rich compositions (x = 0.345, 0.350) and the 14M structure to a further Mn-rich (x = 0.90). As shown in Fig. 10(c), the FSN vector (ξ_1) shifts to 1/5 and further to 1/7 when the system magnetization is increased. For the case of X = Al, the 10M, 12M, and 14M modulations of martensite phases have been observed in the ascending order of the non-stoichiometric compositions (y = 0.40 ~ 0.90)13). In our calculation, the structural modulations may be assigned to the series of peaks for the FSN vectors presented in Fig. 10(a). However, the correspondence between our theoretical results and the experimental ones is not understood in the material trend among X = Al, Ga, and In. Indeed, the modulated structure of 10M or 14M only appears in an intermediate temperature range in the experiments, whereas the low-temperature phase is probably in a spin-glass state, and the structure at high-temperature is the B2 (alloying cubic structure) instead of $L1_2$ (cubic Heusler structure). Thus, the various complex alloying and magnetic effects should be included in the theoretical investigation for X = Al.

4.3 Relationship with the SCAN functional

As described before, the results obtained by the QSGW calculation are comparable to those obtained by the SCAN functional on the calculated magnetic moments (Table 2) and Fermi surface (Fig. 9)33). The one-electron potential in the QSGW includes Coulomb potential with the random phase approximation (the screened Coulomb interaction), whereas the potential of SCAN functional includes some electron localization effects and also provides larger magnetic moments, compared with those of GGA functional52).

5. Conclusions

The properties of electronic structure, such as band dispersion curves, DOS, and generalized susceptibility, Fermi surfaces were investigated using the accurate first-principles calculation of the QSGW method for the cubic Ni_2MnX (X = Al, Ga, In). The electron localization effects on the orbitals at $3d$ transition elements of Ni and Mn are properly introduced in the electronic structures as the random phase approximation. When focusing on the BJT states at the Fermi level, their band width is narrowed, compared with GGA results. According to the results on the DOSs for X = Al and In, the BJT electronic states of minority spin state, appearing just at the Fermi level, were observed to be the same as in the material of X = Ga. The differences on PDOS from their GGA result were comparable to that of X = Ga. On the generalized susceptibility, although the three materials indicate the FSN peak around $2\pi/a$ (0.2, 0.2, 0), its sharpness for X = Al or In was not so remarkable as in the case X = Ga. This is the main difference among the materials and is consistent with the fact that the martensite phase transition takes place only for X = Ga in their stoichiometric composition.

Using the GGA+U approach, the magnetic moments were reproduced by the U parameters on Ni and Mn atoms, resulting in the BJT states to appear just at the Fermi level. However, their band width remains larger than for QSGW, suggesting that such $+U$ approach does not narrow the band width, as expected from this approach. In addition, for X = Al and Ga, the profile of generalized susceptibility does not show a peak at around the wave vectors corresponding to $2\pi/a$ (0.2, 0.2, 0), nor similar to those of QSGW. Even though, GGA+U method can have some similarities with QSGW results, the results do not suggest the same conclusions.

As presented in this work, the current QSGW approach has allowed us to discuss the electronic instabilities mainly caused by the parallel spin states. Discussions on magnetic instability are also interesting to investigate the material properties of Heusler intermetallic compounds.

Appendix A. Fermi surface

Fermi surfaces (FS) of minority spin calculated using GGA (Figures A1(e) and A1(f)) are in agreement with the previously published results for Ni_2MnGa33) and Ni_2MnIn23). Figure A1(d) displays FS for Ni_2MnAl, where the main difference compared to Ni_2MnGa is the part around the Γ point (also visible at the corner). Using the QSGW method, FS changes similarly as if the SCAN functional was applied33) for both Ni_2MnAl and Ni_2MnGa, i.e., the expansion of the portion of the surface corresponding to the lower band (blue) and the shrinking

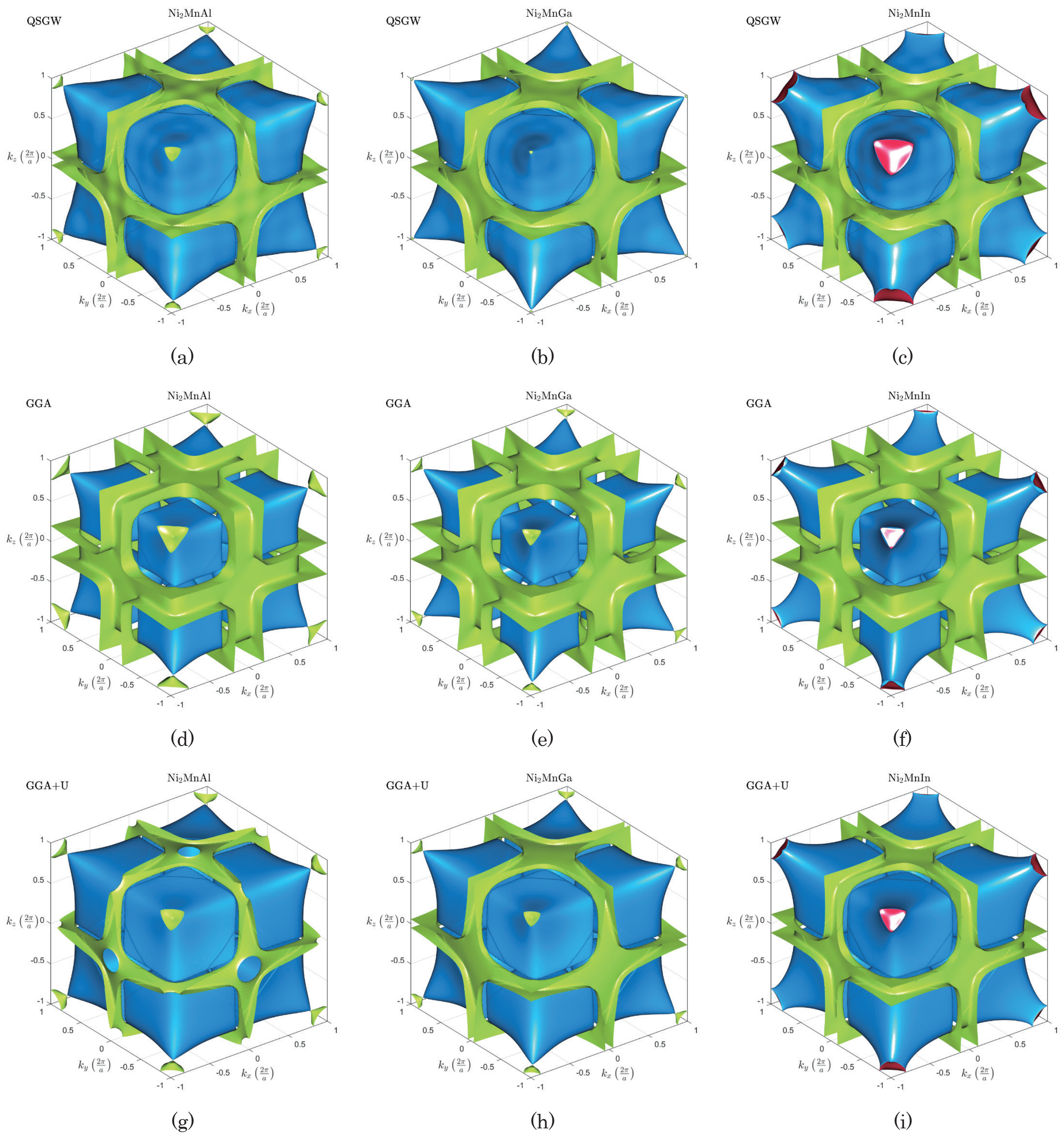

(a) (b) (c)

(d) (e) (f)

(g) (h) (i)

Fig. A1 Comparison among the minority spin Fermi surfaces of Ni_2MnX: QSGW for (a) X=Al, (b) X=Ga, (c) X=In, GGA for (d) X=Al, (e) X=Ga, (f) X=In, GGA + U for (g) X=Al, (h) X=Ga, (i) X=In.

section corresponding to the higher band (green). Using the GGA+U approach resulted in better agreement of FS obtained by this method with QSGW than with GGA for Ni_2MnGa. However, in the case of Ni_2MnAl, the blue band (lower) has a contribution to FS around the X k-point of BZ (Figure A1(g)) for GGA+U, contrary to QSGW, and the size of this part depends on the chosen U parameter. For Ni_2MnIn, the red part of FS which corresponds to the lowest band crossing the Fermi level, expands, as well as the blue part corresponding to the second higher band and the portion related to the highest band shrinks as in the cases of Ni_2MnAl and Ni_2MnGa. FS similarities of Ni_2MnAl and Ni_2MnGa imply that both should also have similar experimental behavior, i.e. the MSM effect should be observed in Ni_2MnAl.

Acknowledgements The author (JL) thanks Petr Sedlák, Hanuš Seiner and Oleg Heczko for valuable discussions on experimental data; the Grant Agency of the Czech Technical University in Prague, grant No. SGS24/146/OHK4/3T/14. The computation was performed at the Supercomputer Center, Institute for Solid State Physics (ISSP), University of Tokyo, Japan. This project was supported by the KAKENHI (No.

21K04864 and No. 21KK0083); and by the FerrMion project of the Czech Ministry of Education, Youth and Sports (project No. CZ.02.01.01/00/22_008/0004591) co-funded by EU.

References

1) K. Ullakko, J. K. Huang, C. Kantner, R. C. O'Handley, and V. V. Kokorin: *Appl. Phys. Lett.*, **69**, 1966 (1996).
2) H. Seiner, M. Zelený, P. Sedlák, L. Straka, and O. Heczko: *Phys. Status Solidi RRL*, **16**, 2100632 (2022).
3) O. Heczko, N. Scheerbaum, and O. Gutfleisch: Magnetic Shape Memory Phenomena, in: Nanoscale Magnetic Materials and Applications, p. 399 (Springer, Boston, 2009).
4) T. Sakamoto, T. Fukuda, T. Kakeshita, T. Takeuchi, and K. Kishio: *J. Appl. Phys.*, **93**, 8647 (2003).
5) M. van Schilfgaarde, T. Kotani, and S. Faleev: *Phys. Rev. Lett.*, **96**, 226402 (2006).
6) M. Zelený, P. Sedlák, O. Heczko, H. Seiner, P. Veřtát, M. Obata, T. Kotani, T. Oda, and L. Straka: *Mater. Des.*, **209**, 109917 (2021).
7) M. Obata, T. Kotani, and T. Oda: *Phys. Rev. Materials*, **7**, 024413 (2023).
8) V. V. Martynov: *J. Phys. IV*, **05**, 91 (1995).
9) V. V. Martynov, and V. V. Kokorin: *J. Phys. III*, **2**, 739 (1992).
10) P. Veřtát, H. Seiner, L. Straka, M. Klicpera, A. Sozinov, O. Fabelo, and O. Heczko: *J. Phys.: Condens. Matter*, **33**, 265404 (2021).
11) R. Chulist, E. Pagounis, P. Czaja, N. Schell, and H.-G. Brokmeier: *Adv. Eng. Mater.*, **23**, 2100131 (2021).
12) M. Zelený, L. Straka, A. Sozinov, O. Heczko: *Phys. Rev. B*, **94**, 224108 (2016).
13) S. Morito, T. Kakeshita, K. Hirata, and K. Otsuka: *Acta Mater.*, **46**, 5377 (1998).
14) M. V. Lyange, E. S. Barmina, and V. V. Khovaylo: *Found. Mater. Sci. Eng.*, **81**, 232 (2015).
15) T. B¨usgen, J. Feydt, R. Hassdorf, S. Thienhaus, M. Moske, M. Boese, A. Zayak, and P. Entel: *Phys. Rev. B*, **70**, 014111 (2004).
16) Y. Sutou, Y. Ohnuma, R. Kainuma, and K. Ishida: *Metall. Mater. Trans. A*, **29**, 2225 (1998).
17) R. Kainuma, K. Ishida, and H. Nakano: *Metall. Mater. Trans. A*, **27**, 4153 (1996).
18) A. Ayuela, J. Enkovaara, K. Ullakko, and R. M. Nieminen: *JJ. Phys.: Condens. Matter*, **11**, 2017 (1999).
19) K Y. Qawasmeh and B. Hamad: *J. Appl. Phys.*, **111**, 033905 (2012).
20) S. Yang, Y. Kong, Y. Du, L. Shen, and Y. Shen: *Comp. Mater. Sci.*, **123**, 52 (2016).
21) S. Chatterjee, V. Singh, A. Deb, S. Giri, S. De, I. Dasgupta, and S. Majumdar: *J. Magn. Magn. Mater.*, **322**, 102 (2010).
22) C. M. Hurd and S. P. McAlister: *J. Magn. Magn. Mater.*, **61**, 114 (1986).
23) M. Siewert, M. E. Gruner, A. Hucht, H. C. Herper, A. Dannenberg, A. Chakrabarti, N. Singh, R. Arróyave, and P. Entel: *Adv. Eng. Mater.*, **14**, 530 (2012).
24) Y. Sutou, Y. Imano, N. Koeda, T. Omori, R. Kainuma, K. Ishida, and K. Oikawa: *Appl. Phys. Lett.*, **85**, 4358 (2004).
25) T. Krenke, M. Acet, E. F. Wassermann, X. Moya, L. Mañosa, and A. Planes: *Phys. Rev. B*, **73**, 174413 (2006).
26) T. Kanomata, T. Yasuda, S. Sasaki, H. Nishihara, R. Kainuma, W. Ito, K. Oikawa, K. Ishida, K.-U. Neumann, and K. Ziebeck: *J. Magn. Magn. Mater.*, **321**, 773 (2009).
27) A. N. Vasilev, A. D. Bozhko, V. V. Khovailo, I. E. Dikshtein, V. G. Shavrov, v. D. Bushelnikov, S. Zuzuki, T. Takagi, and J. Tani: *Phys. Rev. B*, **59**, 1113 (1999).
28) X. Liu, J.-M. Raulot, C. Esling, X. Zhao, and L. Zuo: *J. Magn. Magn. Mater.*, **514**, 167194 (2020).
29) S. Singh, J. Bednarcik, S. R. Barman, C. Felser, and D. Pandey: *Phys. Rev. B*, **92**, 054112 (2015).
30) O. I. Velikokhatnyi and I. I. Naumov: *Phys. Solid State*, **41**, 617 (1999).
31) Y. Lee, J. Y. Rhee, and B. N. Harmon: *Phys. Rev. B*, **66**, 054424 (2002).
32) C. Bungaro, K. M. Rabe, and A. D. Corso: *Phys. Rev. B*, **66**, 134104 (2003).
33) D. R. Baigutlin, V. V. Sokolovskiy, O. N. Miroshkina, M. A. Zagrebin, J. Nokelainen, A. Pulkkinen, B. Barbiellini, K. Pussi, E. L¨ahderanta, V. D. Buchelnikov, and A. T. Zayak: *Phys. Rev. B*, **102**, 045127 (2020).
34) J. Janovec, M. Zelený, O. Heczko, and A. Ayuela: *Sci. Rep.*, **12**, 20577 (2022).
35) S. V. Faleev, M. van Schilfgaarde, and T. Kotani: *Phys. Rev Lett.*, **93**, 126406 (2004).
36) T. Kotani, M. van Schilfgaarde, and S. V. Faleev: *Phys. Rev. B*, **76**, 165106 (2007).
37) T. Kotani: *J. Phys. Soc. Jpn.*, **83**, 094711 (2014).
38) J. P. Perdew, K. Burke, and M. Ernzerhof: *Phys. Rev. Lett.*, **77**, 3865 (1996).
39) A. L. Liechtenstein, V. I. Anisimov, and J. Zaanen: *Phys. Rev. B*, **52**, 5467 (1995).
40) https://github.com/tkotani/ecalj/ (As of April, 2024).
41) Y. Lee, T. Kotani, and L. Ke: *Phys. Rev. B*, **101**, 241409 (2020).
42) K. R. A. Ziebeck and P. J. Webster: *J. Phys. F: Met. Phys.*, **5**, 1756 (1975).
43) P. J. Webster, K. R. A. Ziebeck, S. L. Town, and M. S. Peak: *Philos. Mag. B*, **49**, 295 (1984).
44) K. Motizuki, Structural phase transitions in layered transition metal compounds, p. 11-14 (D. Reisel Publishing Company, Dordrecht, Holland,1986). The contribution from the second-order partial derivatives of the transfer integral with respect to atomic position, D_2, appearing in the general approach (see the corresponding page above), was excluded from the present investigation because of both its resulting short range atomic forces and temperature-independent feature.
45) Q.-M. Hu, C.-M. Li, S. E. Kulkova, R. Yang, B. Johansson, and L. Vitos: *Phys. Rev. B*, **81**, 064108 (2010).
46) T. Koubský, P. Sedlák, H. Seiner, J. Fojtíková, M. Obata, T. Oda, and L. Kalvod: *Acta Phys. Pol. A*, **134**, 804 (2018).
47) L. Sponza, P. Pisanti, A. Vishina, D. Pashov, C. Weber, M. van Schilfgaarde, S. Acharya, J. Vidal, and G. Kotliar: *Phys. Rev. B*, **95**, 041112 (2007).
48) Y. Takahashi: *J. Phys. Soc. Jpn.*, **55**, 3553 (1986).
49) C. P. Opeil, B. Mihaila, R. K. Schultz, L. Mañosa, A. Planes, W. L. Hults, R. A. Fisher, P. S. Riseborough, P. B. Littlewood, J. L. Smith, and J. C. Lashley: *Phys. Rev. Lett.*, **100**, 165703 (2008).
50) A. Kimura, M. Ye, M. Taniguchi, E. Ikenaga, J. M. Barandiarán, and V. A. Chernenko: *Appl. Phys. Lett.*, **103**, 072403 (2013).
51) T. Krenke, E. Duman, M. Acet, E. F. Wassermann, X. Moya, L. Mañosa, A. Planes, E. Suard, and B. Ouladdiaf: *Phys. Rev. B*, **75**, 104414 (2007).
52) F. Tran, G. Baudesson, J. Carrete, G. K. Madsen, P. Blaha, K. Schwarz, and D. J. Singh: *Phys. Rev. B*, **102**, 024407 (2020).

Received Apr. 25, 2024; Accepted July 16, 2024

INDEX

J. Magn. Soc. Jpn., **48**, 108-111 (2024) <Paper>

Analysis of magnetic anisotropy constants obtained from Hall data using generalized Sucksmith Thompson method on $NiCo_2O_4$(001) films with tilted preferential direction

H. Koizumi*, and H. Yanagihara**
Department of Applied Physics, University of Tsukuba, *Tsukuba, Ibaraki 305-8573, Japan*
*Center for Science and Innovation in Spintronics (CSIS), Tohoku University, Sendai 980-8577, Japan.
**Tsukuba Research Center for Energy Materials Science (TREMS), University of Tsukuba, *Tsukuba, Ibaraki 305-8573, Japan*

We investigated the magnetic anisotropy of $NiCo_2O_4$ thin film with a relatively large second-order magnetic anisotropy, which gives rise to easy-cone magnetic anisotropy. Anomalous Hall data measured in external magnetic fields at various angles were analyzed based on the generalized Sucksmith-Thompson (GST) method to quantitatively extract both the first- and second-order anisotropy constants. Although the GST model is valid for any external field angle, we found that the analysis was useful only when the field was either parallel or normal to the film plane. However, the tilted magnetic field results show the effect of misalignment between the actual and expected angles of the field. Our results indicate the validity of estimating higher-order magnetic anisotropy and adjusting the misalignment of measurement systems.

Keywords: magnetic anisotropy, thin film, Hall effect

1. Introduction

Magnetic anisotropy is a key physical parameter that characterizes magnetic materials and determines the preferential direction of magnetization. According to the phenomenological model, the free energy of uniaxially anisotropic systems such as hexagonal and tetragonal crystal structures can be expressed as $E_{\mathrm{MA}} = K_{u1}\sin^2\theta + K_{u2}\sin^4\theta + \cdots$1). Here, K_{u1} and K_{u2} denote the uniaxial magnetic anisotropy constants for the first- and second-order terms, respectively, and θ indicates the angle between the uniaxial axis and magnetization. In most magnetic materials, K_{u1} is dominant in determining the preferential direction of magnetization, which is parallel to the crystal's primitive crystallographic direction with the simple index. When $-2K_{u2} < K_{u1} < 0$, the preferential magnetization direction is tilted from a uniaxial axis corresponding to a primitive crystallographic direction. The tilted state of the magnetization alignment is called easy-cone magnetic anisotropy (ECMA) 2–4), in which the tilt angle is expressed as $\theta_c = \sin^{-1}\sqrt{-K_{u1}/2K_{u2}}$. Recently, some studies have proposed that ECMA assists the magnetization switching process via a spin-transfer torque5–9) and allows unique easy-cone domain wall dynamics10). Thus, the role of K_{u2} in magnetization processes has been re-identified, and quantitative treatment of K_{u2} is required not only for ECMA but also for the magnetic dynamics of perpendicular magnetic anisotropy (PMA) materials.

Because the ECMA is attributed to the higher-order term of the magnetic anisotropy constants, its confirmation is not straightforward. In most cases, ECMA is identified using magneto-torque or ferromagnetic resonance measurements by determining both K_{u1} and K_{u2} 1,11). The method to determine K_{u1} and K_{u2} from the magnetization curves developed by Sucksmith-Thompson and others12,13) can be generalized for any arbitrary field direction. When a magnetic field is applied along a certain direction, the magnetic free energy, composed of both the magnetic anisotropy and Zeeman energies, is expressed as:

$$E = K_{u1}^{\mathrm{eff}}\sin^2\theta + K_{u2}\sin^4\theta - \mu_0 H M_S\cos(\theta - \theta_H), \qquad (1)$$

K_{u1}^{eff} is the sum of the two contributions from K_{u1} and shape anisotropy. θ and θ_H represent the angles of the direction pointing to the magnetization and the applied field measured from the uniaxial axis, respectively. M_S is the saturation magnetization. As the equilibrium condition of the torque components derived from Eq. (1), i.e. $\partial E/\partial\theta = 0$, the GST formula can be expressed as:

$$\left(2K_{u1}^{\mathrm{eff}} + 4K_{u2}\right)/M_S - 4K_{u2}\cos^2\theta/M_S = \gamma\mu_0 H, \qquad (2)$$

$$\gamma \equiv (\cos\theta\sin\theta_H - \sin\theta\cos\theta_H)/\sin\theta\cos\theta. \qquad (3)$$

$NiCo_2O_4$(NCO) is a conductive ferrimagnet with a relatively high Néel temperature of $T_N \approx 400$ K14). NCO(001) films grown on $MgAl_2O_4$ (MAO) substrates exhibit PMA at room temperature due to compressive strain15–17). Moreover, NCO(001) films exhibit strong ECMA at low temperatures, and semi-quantitative calculations have revealed that the anti-site distribution of Ni^{3+} at the T_d site denotes the origin of the ECMA18). Recently, the characteristic Hall effect, termed the quadrupole anomalous Hall effect (QuadAHE), was demonstrated in NCO(001) film, which is correlated with ECMA19). The spin-reorientation temperature (T_{SR}) at which the magnetic anisotropy changes from PMA to

---

Corresponding author:
H. Koizumi (e-mail: hiroki.koizumi.d7@tohoku.ac.jp),

ECMA strongly depends on the film fabrication conditions.

In this study, we examined the applicability of GST analysis to anomalous Hall (AHE) data measured at various angles on the epitaxial NCO(001) film exhibiting ECMA, meaning that K_{u2} is relatively large.

2. Experiment

Epitaxial NCO(001) films with a thickness of 42 nm were grown by reactive radio frequency magnetron sputtering technique. A 2-inch alloy target with a nominal composition of Ni: Co = 1: 2 was used. The growth conditions of the NCO film were as follows: the Ar and O_2 flow rates were set to 10 and 2.5 sccm, respectively; the process temperature was 300˚C, and the working pressure was 1.3 Pa. Subsequently, the NCO film was annealed at 300˚C for 10 min under an oxygen pressure of 0.2 Pa. The films were patterned into Hall bars using photolithography and Ar ion milling to perform electric transport measurements. Hall measurements were performed using a physical property measurement system (PPMS, Quantum Design) with a DC source (Keithley 6221) and a nanovoltmeter (Keithley 2182).

3. Results and discussion

3.1 Hall measurements

According to Eqs. (2) and (3), the magnetic hysteresis or AHE curves measured at various angles of θ_H are useful for performing the GST method. Next, Hall measurements were performed in tilted magnetic fields to extract both K_{u1}^{eff} and K_{u2}.

Figure 1 shows Hall data ρ_H under different tilted magnetic fields with the angle θ_H ranging from $\theta_H = 0$ to $\theta_H = 90°$ determined from normal to the film plane to NCO[100] at 10 K. ρ_H consist of ordinary Hall effect (OHE) and AHE, resistivity. The OHE is proportional to the normal component of the field, i.e., $\rho_{\mathrm{OHE}} = \mu_0 R_0 H \cos\theta_H$, where R_0 is the ordinary Hall coefficient. Based on the experimental results of $\theta_H = 0$, R_0 is $-3 \times 10^{-11}\ m^3/\mathrm{C}$ ($= -0.003$ μΩcm/T). Therefore, ρ_{AHE} components can be extracted from ρ_H as, $\rho_{\mathrm{AHE}}(\theta_H) = \rho_H(\theta_H) - \mu_0 R_0 H \cos\theta_H$ in principle. Since ρ_{OHE} is "negligibly small" compared with ρ_{AHE} in NCO films, $\rho_{\mathrm{AHE}}(\theta_H)$ behavior is almost same with ρ_H. In the subsequent analysis, we used the extracted AHE data.

Although the high field behavior of ρ_{AHE} depends significantly on the applied field angle, the remanence of the Hall resistivity corresponding to remanent ρ_{AHE} is almost independent of the field angle. This is consistent with the simulation results obtained using a coherent rotation model (not shown), in which all magnetic moments rotate simultaneously without magnetic domains under ECMA conditions [20,21].

3.2 GST analysis

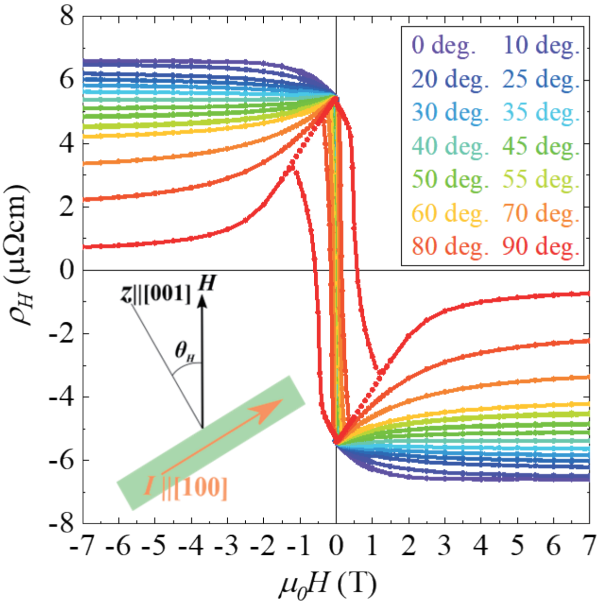

Fig. 1 Applied field angle (θ_H) dependence of Hall resistivity at 10 K. The tilted direction is from NCO[001] to NCO[100].

Next, we performed GST analysis on the field-angle-dependent AHE data to evaluate K_u's. As expressed in Eq. (1), the GST method was established for uniaxial magnetic anisotropic materials. Bulk NCO possesses a cubic structure; however, our NCO films are suffering from in-plane compressive stresses owing to lattice mismatch between the film and substrate. Consequently, the characteristic properties, including the magnetic properties of the film, exhibit tetragonal symmetry rather than cubic symmetry. In fact, the magnetic anisotropy of NCO films, such as PMA and ECMA, is uniaxial. Therefore, the GST method can be reasonably applied to analyze magnetic anisotropy.

In the GST analysis, we used the AHE data of the decreasing field in the positive region. θ in Eq. (2) corresponds to the magnetization angle from the uniaxial axis, which is parallel to NCO[001]. Therefore, $\cos\theta$ corresponds to the normalized AHE, i.e., $\cos\theta = \rho_{\mathrm{AHE}}(\theta_H)/\rho_{\mathrm{AHE}}(\theta_H = 0, \text{saturation})$. The GST plot of $\gamma\mu_0 H$ versus $\cos^2\theta$ for $0° \le \theta_H \le 90°$ is shown in Fig. 2, where the slope and the vertical axis intercept on this plot correspond to $-4K_{u2}/M_S$ and $\left(2K_{u1}^{\mathrm{eff}} + 4K_{u2}\right)/M_S$, respectively. Accordingly, the magnetic anisotropy constants can be estimated by substituting the M_S which is determined separately by magnetization measurement. In addition, the horizontal axis intercept agrees with the easy-cone angle (θ_c), because $\cos^2\theta_c = (2K_{u1}^{\mathrm{eff}} + 4K_{u2})/4K_{u2}$. As Eq. (2) holds an arbitrary angle, all the AHE data collapse on a single straight line on the GST plot.

As observed, the GST analysis results from AHE data are linear below $|\mu_0 H| \approx 1$ T in $\theta_H = 0$ and 90 degrees. Assuming $M_S = 2$ μB/f.u., from the linear fitting results

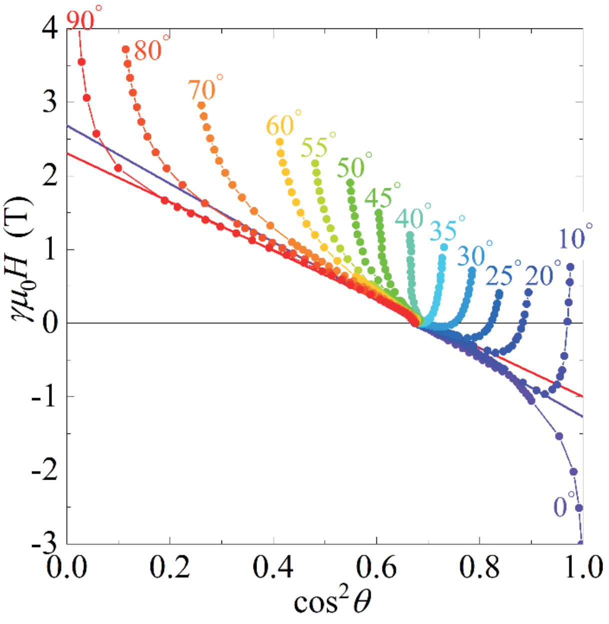

Fig. 2 $\gamma\mu_0 H$ versus $\cos^2\theta$ plots from 0° to 90°. The purple and red lines are linear fitting results of 0° and 90° degrees. According to the GST model, the slope and the intercept of the vertical axis correspond to $-4K_{u2}/M_S$ and $\left(2K_{u1}^{\mathrm{eff}} + 4K_{u2}\right)/M_S$, respectively.

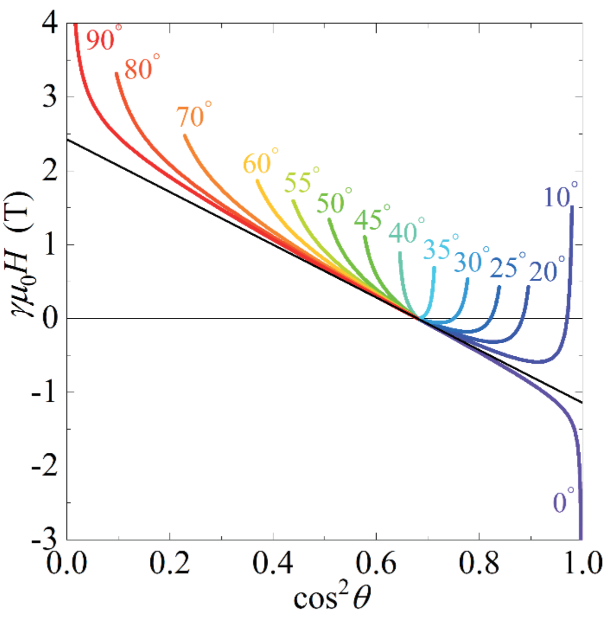

Fig. 3 Macro-spin calculation results $\gamma\mu_0 H$ versus $\cos^2\theta$ plots from 0° to 90° degrees with −3° misalignment. The plot color corresponds to the Fig. 2.

of 0 and 90 degrees shown in the purple and red line, $K_{u1}^{\mathrm{eff}} = -0.17, -0.14$ and $K_{u2} = 0.27, 0.23$ MJ/m^3, respectively. In contrast, the GST results of $\theta_H \neq 0, 90$ degrees show significant discrepancies from the linear fitting results. Moreover, larger discrepancies are observed when a large external field is applied. Thus, it is difficult to obtain accurate values from tilted field results. However, the horizontal axis intercept, which corresponds to the easy-cone angle, agreed with all the measured angles. Hence, the discrepancy gradually appeared in the high field region, except for perpendicular and parallel to the plane.

3.3 Numerical calculation

We performed numerical calculations for the angle-dependent AHE. The calculation parameters were as follows; $M_S = 280$ kA/m, $K_{u1} = -0.16$, and $K_{u2} = 0.25$ MJ/m^3. The magnetic hysteresis was obtained by calculating the lowest energy using Eq. (1). When GST analysis was performed on the calculation results, all the results appeared on one straight line regardless of the angle, as shown by the black line in Fig. 3.

To consider the origin of the discrepancies, we assumed that misalignment occurred between the actual and expected angles of the external magnetic field, i.e. $\theta_H \to \theta_H + \delta$. Then, γ is modified to $2\sin(\theta_H + \delta - \theta)\,/\sin 2\theta$. By assuming $\cos\delta \approx 1$, $\mu_0 H \cos(\theta_H - \theta)\sin\delta\,/\sin 2\theta$ is added to the right-hand side of Eq. (2). The effect of the additional term was apparent particularly in the high field region owing to $\theta \approx \theta_H$. Figure 3 shows the calculated GST results based on a misalignment of $\delta = -3°$. The plotted angles and colors correspond to the experimental results shown in Fig. 2. The behavior of the misaligned GST plots was consistent with the experimental results. Therefore, the discrepancies in the GST analysis were primarily caused by the angular misalignment of the external magnetic field.

These considerations suggest that GST analysis can be performed to estimate the angular misalignment of the measurement system because the GST plot is sensitive to slight changes in the hysteresis curve.

4. Conclusion

In summary, we fabricated an epitaxial NCO film on an MAO(001) substrate, which is known to exhibit strong ECMA at low temperatures. From the field-angle dependence of the AHE, we performed a GST analysis and attempted to estimate the magnetic anisotropy constants up to the second order. The analysis results did not appear to follow the GST method in the high field region with the tilted field. The angular misalignment of the external magnetic field partially explains one of the origins of the discrepancies. These results showed the difficulty of GST analysis in more general cases and the high sensitivity of misalignment of the experimental system.

Acknowledgements This project was partly supported by KAKENHI (21H01750, 22H04966, 23H01842) and TIA-Kakehashi (TK22-023, TK-23-017). The microfabrication in this work was carried out under the MEXT program of Advanced Research Infrastructure for Materials and Nanotechnology in Japan

(JPMXP1222BA0017) with the cooperation of T. Kashiwagi and the Nanotechnology Platform at the University of Tsukuba. H. K. acknowledges the support of Grant-in-Aid for JSPS Fellows (20J10749 and 22J00871).

References

1) S. Chikazumi and C. D. Graham: *Physics of Ferromagnetism*. (Oxford University Press, 1997).
2) J. M. Shaw, H. T. Nembach, M. Weiler, T. J. Silva, M. Schoen, J. Z. Sun, and D. C. Worledge: *IEEE Magn. Lett.*, **6**, 3500404 (2015).
3) A. A. Timopheev, R. Sousa, M. Chshiev, H. T. Nguyen, and B. Dieny: *Sci. Rep.*, **6**, 26877 (2016).
4) Y. He, G. H. Fecher, J. Kroder, H. Borrmann, X. Wang, L. Zhang, C. Y. Kuo, C. E. Liu, C. Te Chen, K. Chen, F. Choueikani, P. Ohresser, A. Tanaka, Z. Hu, and C. Felser: *Appl. Phys. Lett.*, **116**, 102404 (2020).
5) R. Matsumoto, H. Arai, S. Yuasa, and H. Imamura: *Phys. Rev. B*, **92**, 140409 (2015).
6) R. Matsumoto, H. Arai, S. Yuasa, and H. Imamura: *Appl. Phys. Express*, **8**, 063007 (2015).
7) N. Strelkov, A. Timopheev, R. C. Sousa, M. Chshiev, L. D. Buda-Prejbeanu, and B. Dieny: *Phys. Rev. B*, **95**, 184409 (2017).
8) O. Bultynck, M. Manfrini, A. Vaysset, J. Swerts, C. J. Wilson, B. Sorée, M. Heyns, D. Mocuta, I. P. Radu, and T. Devolder: *Phys. Rev. Appl.*, **10**, 054028 (2018).
9) M. Lavanant, S. Petit-Watelot, A. D. Kent, and S. Mangin: *Appl. Phys. Lett.*, **114**, 012404 (2019).
10) P. H. Jang, S. H. Oh, S. K. Kim, and K. J. Lee: *Phys. Rev. B*, **99**, 024424 (2019).
11) M. Farle: *Rep. Prog. Phys.*, **61**, 755 (1998).
12) W. Sucksmith and J. E. Thompson: *Proc. R. Soc. A*, **225**, 362 (1954).
13) A. S. Bolyachkin, D. S. Neznakhin, and M. I. Bartashevich: *J. Appl. Phys.*, **118**, 213902 (2015).
14) P. D. Battle, A. K. Cheetham, and J. B. Goodenough: *Mater. Res. Bull.*, **14**, 1013 (1979).
15) X. Chen, X. Zhang, M. G. Han, L. Zhang, Y. Zhu, X. Xu, and X. Hong: *Adv. Mater.*, **31**, 1805260 (2019).
16) C. Mellinger, J. Waybright, X. Zhang, C. Schmidt, and X. Xu: *Phys. Rev. B*, **101**, 014413 (2020).
17) D. Kan, M. Mizumaki, M. Kitamura, Y. Kotani, Y. Shen, I. Suzuki, K. Horiba, and Y. Shimakawa: *Phys. Rev. B*, **101**, 224434 (2020).
18) H. Koizumi, I. Suzuki, D. Kan, J. I. Inoue, Y. Wakabayashi, Y. Shimakawa, and H. Yanagihara: *Phys. Rev. B*, **104**, 014422 (2021).
19) H. Koizumi, Y. Yamasaki, and H. Yanagihara: *Nat. Commun.*, **14**, 8074 (2023).
20) E. C. Stoner and E. P. Wohlfarth: *Philos. Trans. R. Soc. A*, **240**, 599 (1948).
21) J. M. D. Coey: *Magnetism and Magnetic Materials*. (Cambridge University Press, 2010).

Received Feb. 29, 2024; Revised May 20, 2024; Accepted Jul. 23 2024

INDEX

J. Magn. Soc. Jpn., **48**, 112-115 (2024)

<Letter>

Influence of Stray Field on Magnetization Switching Induced by Spin-Orbit Torque

F. Ye[1], H. Jang[1], Y. Shiota[1,2], H. Narita[1], R. Hisatomi[1,2], S. Karube[1,2], S. Sugimoto[3], S. Kasai[3], T. Ono[1,2]
[1]Institute for Chemical Research, Kyoto University, *Gokasho, Uji, Kyoto 611-0011, Japan*
[2]Center for Spintronics Research Network, Kyoto University, *Gokasho, Uji, Kyoto 611-0011, Japan*
[3]National Institute for Materials Science (NIMS), *1-2-1 Sengen, Tsukuba, Ibaraki 305-0047, Japan*

In a vertical domain wall motion memory with artificial ferromagnets, magnetization switching induced by spin-orbit torque (SOT) is employed for the data-writing method. This data-writing process may suffer from stray fields from the reference layer; however, this effect has been rarely addressed so far. In this study, we investigated the relationship between the critical current density required for SOT-induced magnetization switching and the stray field by varying the ferromagnetic layer thickness of synthetic antiferromagnetic reference layers in nanopillars with diameters of 300 nm and 200 nm. The results reveal that the critical current density is little affected by changes in the stray field in our system.

Keywords: domain wall motion memory, stray field, hysteresis, spin-orbit torque, thickness dependence

1. Introduction

Domain wall (DW) motion in magnetic nanowires has attracted considerable interest due to its non-volatility and potential for high-density integration[1)–3)]. In the DW motion memory, logic bits are stored in magnetic domains and separated by DWs. By injecting electric currents, these logic bits can be moved to desired storage position due to the motion of the DWs[4),5)].

For practical applications, high thermal stability is crucial to retain the magnetization direction against external disturbance considering the data security. The thermal stability factor Δ of a magnetic memory device can be described by $\Delta = E_{\mathrm{b}}/(k_{\mathrm{B}}T)$, where E_{b}, k_{B}, and T are the energy barrier, the Boltzmann constant, and the temperature. On the other hand, a low critical current (J_c) to drive the DW motion is necessary to minimize electricity consumption and heat generation. However, there exists a dilemma between maintaining the thermal stability of data and achieving the low operation current. Enhancing E_{b} improves thermal stability but simultaneously increases the critical current density[6)].

To address this issue, a novel vertical DW motion memory with artificial ferromagnets exhibiting perpendicular magnetic anisotropy (PMA) was designed in our previous works[7),8)]. In this memory cell, data bits are written into the bottommost ferromagnetic layer by injecting in-plane currents through the heavy metal bottom electrode to induce spin-orbit torque (SOT)[9)–13)]. Then, the bits can be shifted to upper layers by spin-transfer torque (STT) through out-of-plane pulse injection[14)–16)]. Micromagnetic simulations have shown that by tuning the properties of each layer, it is possible to achieve both a low critical current density ($J_c < 10^{11}$ A m^{-2}) and high thermal stability ($\Delta > 60$)[8)].

However, in this structure, the stray field from the other layers may affect the memory operation in data-writing and shift processes[17)]. In this study, we investigated the influence of stray field on the SOT-induced magnetization switching for the writing process in nanopillars with PMA.

2. Experimental results

2.1 Device fabrication

Multilayers of Ta(5) / Pt(10) / Co(1.4) / Cu(3) / Co(0.8) / Pt(0.8) / Co(0.8) / Ru(0.75) / Co(0.8) / Pt(0.8) / Co(t_{Co}: 0.4-1.0) / Pt(3) were deposited on thermally oxidized Si substrate using sputtering as shown in Fig. 1(a). The numbers in parentheses are the thickness of each layer in nanometers. The bottom 10-nm-thick Pt layer was utilized for the bottom electrode to induce SOT. The 3-nm-thick Cu layer is a spacer layer between free layer and synthetic antiferromagnet (SAF) to read out the information of magnetization configuration through the giant magnetoresistance (GMR) effect. SAF structure was used as a reference layer of memory cells to reduce

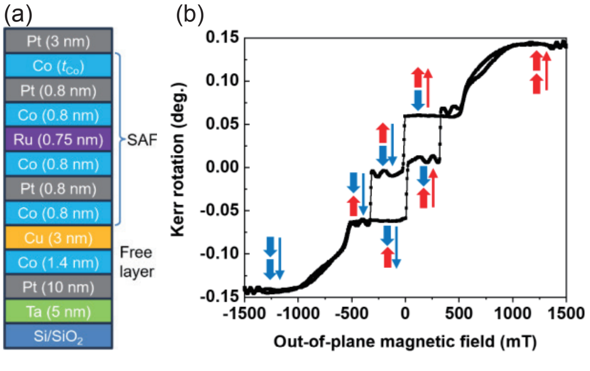

Fig. 1 (a) Schematic illustration of multilayer structure. (b) Polar-Kerr hysteresis loop of sample with $t_{\mathrm{Co}} = 0.72$ nm. Thick and thin arrows represent magnetization of SAF layer and the free layer, respectively.

Corresponding author:
T. Ono (e-mail: ono@scl.kyoto-u.ac.jp).

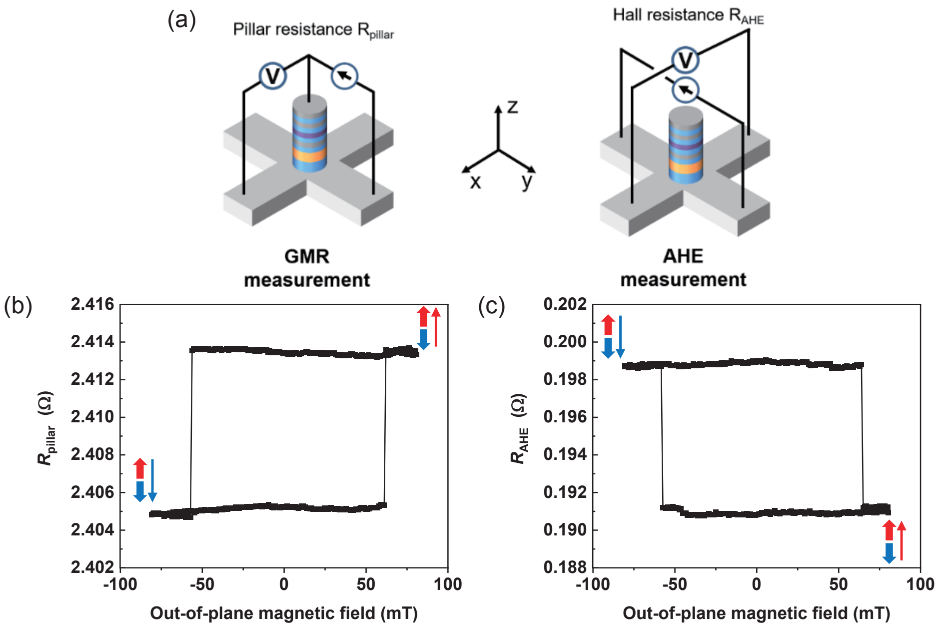

Fig. 2 (a) Schematic of experimental setup for GMR and AHE measurements. (b) Pillar resistance R_{pillar} and (c) Hall resistance R_{AHE} as a function of out-of-plane magnetic field, respectively, in 300 nm device.

the stray field[18], which may suppress the efficiency of SOT-induced magnetization switching. In SAF structure, the net magnetization in the antiparallel magnetization configuration depends on the thickness ratio of two ferromagnetic layers. Therefore, the wedge-shaped Co layer was made to vary the strength of stray field. Figure 1(b) shows the polar-Kerr hysteresis loop of the sample with t_{Co} = 0.72 nm, indicating that the magnetization of the free layer switches in smaller magnetic field than that of the SAF layer.

This film was fabricated into nanopillars with 300 nm and 200 nm diameters by electron beam lithography and Ar ion etching. The Pt bottom layer was patterned into a 1-µm-wide stripe, and the rest of the layers were etched to form a nanopillar on the Pt bottom layer. The etchings depth was monitored by in-situ secondary ion mass spectroscopy for the endpoint detection. The hysteresis of the devices was measured by GMR effect and anomalous Hall effect (AHE) by sweeping an out-of-plane magnetic field using the experimental setup shown in Fig. 2(a). A 0.5 mA DC current was applied by a current source, and the pillar resistance R_{pillar} and Hall resistance R_{AHE} were evaluated from corresponding voltages.

2.2 Hysteresis measurements

Minor hysteresis loops measured by a 300 nm pillar with t_{Co} = 0.91 nm are shown in Figs. 2(b) and 2(c). The magnetization configurations of each state are represented by arrows in the figure. Square hysteresis with sharp resistance changes indicate that the free layer has a perpendicular easy axis with sufficiently large PMA. In the AHE measurements, the switching signal appears at a magnetic field almost identical to that in the GMR measurements, suggesting that this resistance change also arises from the switching of the free layer.

It should be noted that in the antiparallel magnetization configuration of the SAF structure, the magnetization of the Co/Pt/Co layer with a larger total magnetic moment should be oriented in the magnetic field direction because it is more stable to reduce the Zeeman energy. In our sample, the thickness of the lower Co/Pt/Co layer is fixed. Thus, in case of small t_{Co}, the magnetic moment of the SAF is dominated by the lower Co/Pt/Co layer and vice versa. This means that there exists a Co thickness such that the magnetization of the upper and lower Co/Pt/Co layers exactly cancels out. For the devices on two sides of this thickness, their magnetizations of SAFs should orient in opposite directions. This difference can be examined by GMR curves. Figures 3(a) and 3(b) show the hysteresis of 300 nm devices with t_{Co} = 0.55 nm and 0.58 nm. Two hysteresis loops show opposite polarities that the low-(high-)resistance states were obtained for the device with t_{Co} = 0.55 nm (0.58 nm) at large positive field, respectively. Since the free layer magnetization is now oriented in the $+z$ direction, the magnetization configuration of the SAF structure can be deduced from the resistance states of R_{pillar} as represented by arrows in the figure. The results of Figs. 3(a) and 3(b) reveal that the Co thickness at which the antiparallel magnetization configuration of the SAF structure is inverted is approximately between 0.55 and 0.58 nm. This thickness is smaller than the expected thickness of t_{Co} = 0.8 nm from the symmetry of the film structure. This discrepancy can be attributed to the contribution of the magnetization induced in the top Pt capping layer through the proximity effect[19),20)].

We then measured the minor hysteresis loops of devices with various t_{Co} to estimate the hysteresis shift, which is the shift of the center field of the free layer

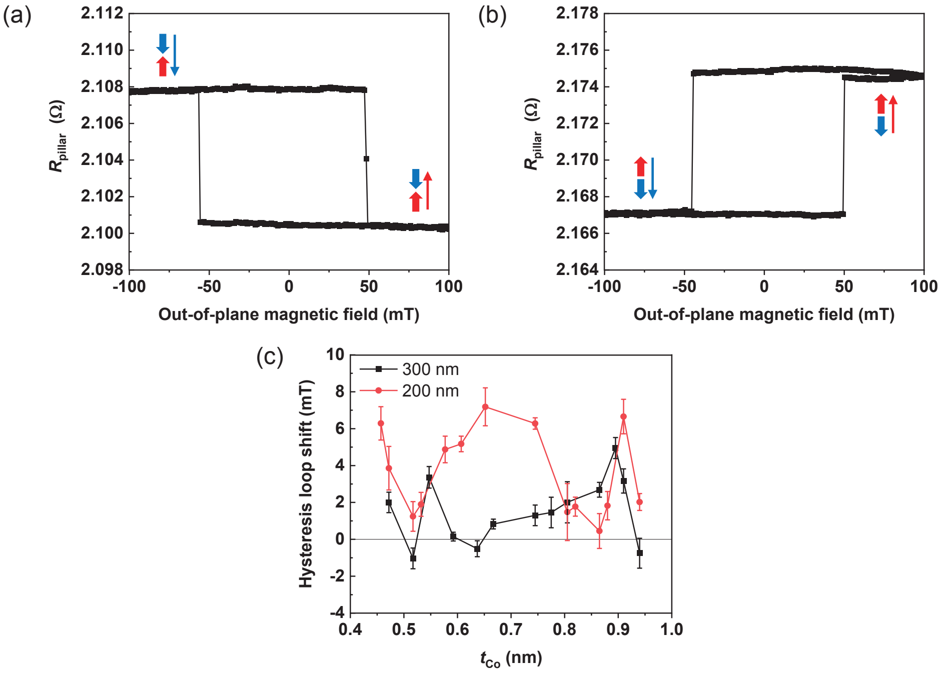

Fig. 3 (a) (b) Out-of-plane magnetic field dependence of R_{pillar} measured using 300-nm devices with (a) t_{Co} = 0.55 nm and (b) t_{Co} = 0.58 nm, respectively. (c) Co thickness dependence of hysteresis loop shift.

hysteresis loops. For each device, 10 measurement cycles were performed to evaluate the average value of switching fields to minimize the effect of thermal fluctuation. The magnetizations of the SAF structure were set to the same configuration as represented in Fig. 3(b) before the measurements. Figure 3(c) shows the evaluated hysteresis loop shift as a function of t_{Co}. We expected the hysteresis loop shift to vary monotonically with respect to the t_{Co}. However, in 300 nm and 200 nm devices, the hysteresis loop shift does not show a clear trend with respect to t_{Co} and is positive in most devices. This may be because the stray field is more sensitive to the microfabrication imperfection than to the variation of the Co thickness in SAF structure. Hereafter, we assume that this hysteresis loop shift corresponds to the stray field to the free layer21).

2.3 SOT-induced magnetization switching

Next, we investigated the influence of stray field on SOT-induced magnetization switching. In the experiments, in-plane current pulses with 20 ms pulse duration were injected to the bottom Pt electrode to generate spin current originating from the spin-Hall effect. AHE resistance which is proportional to the out-of-plane component of the magnetization was measured under a 0.5 mA DC current. An in-plane magnetic field is applied to break the mirror symmetry22). In all measurements, the magnetization configurations in SAF structure were also set to be the same configuration as represented in Fig. 3(b). Figure 4(a) shows the SOT switching loops of a 300 nm pillar with t_{Co} = 0.91 nm, where ΔR_{AHE} is calculated by subtracting the R_{AHE} offset. The change in ΔR_{AHE} reflects the complete switching of the free layer magnetization as shown in Fig. 2(c). When the direction of the in-plane magnetic field is reversed, the loop polarity also changes, which is a distinct feature of SOT-induced switching.

The Co thickness dependence of the critical current of SOT switching was studied with the application of a +50 mT in-plane magnetic field. To facilitate comparisons between different devices, we define J_c as the current density when the change in resistance is 20% of the full resistance change in the hysteresis measured by AHE, because several samples exhibited a reduced ΔR_{AHE} in the SOT switching loop compared to that observed in the hysteresis. The positive critical current density J_c and the absolute value of the negative critical current density $|-J_c|$ are plotted as a function of t_{Co} in Figs. 4(b) and 4(c), where the J_c was evaluated from the average value from 10 repeated measurements. Then the SOT loop shift was evaluated from $(J_c - |-J_c|)/2$.

To investigate the influence of the stray field on the SOT-induced magnetization switching, we plotted the relationship between the SOT loop shifts and hysteresis loop shifts in Fig. 4(d). From this result, we find little correlation between them for both the 300 nm and 200 nm devices, despite there is a larger deviation in the 200 nm devices compared to the 300 nm devices due to microfabrication imperfections. This implies that the response of the critical current density to changes in the stray field is insensitive in our system. A plausible explanation is that, unlike the situation with the direct application of an external magnetic field, the stray field from the reference layer in the nanopillar may exhibit an inhomogeneous distribution across the free layer. This leads to the experimental results differing from our expectation that the SOT loop shifts and hysteresis loop shifts would show a clearer correlation.

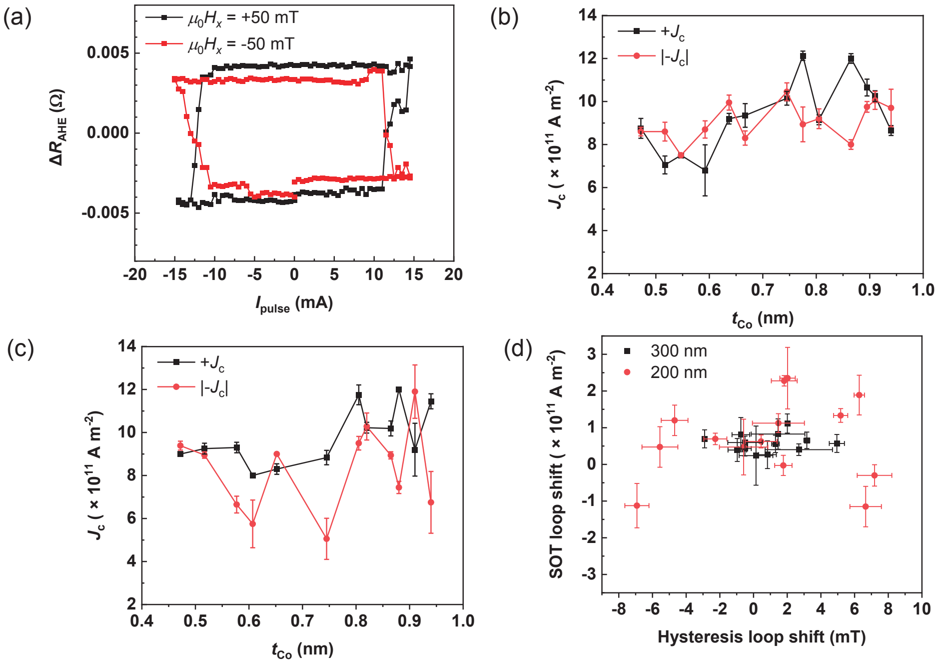

Fig. 4 (a) SOT-induced magnetization switching under in-plane magnetic field of ±50 mT using 300-nm device with t_{Co} = 0.91 nm. (b) (c) Co thickness dependence of J_c and $|-J_c|$ in diameter of (b) 300-nm and (c) 200-nm nanopillars. (d) Relationship between hysteresis loop shift and SOT loop shift.

3. Conclusion

We investigated the critical current density of SOT-induced free-layer magnetization switching in nanopillars of 300 nm and 200 nm diameters, with reference SAF layers of different Co thickness. Within the range of stray fields observed in our hysteresis measurements, we found that there is little correlation between the critical current density and the stray field.

Acknowledgements This work was partly supported by JST-CREST Grant Number JPMJCR21C1, MEXT Initiative to Establish Nest-generation Novel Integrated Circuits Center (X-NICS) Grant Number JPJ011438, JST, the establishment of university fellowships towards the creation of science technology innovation, Grant Number JPMJFS2123, Cooperative Research Project Program of the Research Institute of Electrical Communication, Tohoku University, and Collaborative Research Program of the Institute for Chemical Research, Kyoto University.

References

1) S. Parkin, X. Jiang, C. Kaiser, A. Panchula, K. Roche, and M. Samant, *Proc. IEEE*, **91**, 661 (2003).
2) S. S. P. Parkin, M. Hayashi, and L. Thomas, *Science*, **320**, 190 (2008).
3) S.-H. Yang, K.-S. Ryu, and S. Parkin, *Nat. Nanotechnol.*, **10**, 221 (2015).
4) A. Yamaguchi, T. Ono, S. Nasu, K. Miyake, K. Mibu, and T. Shinjo, *Phys. Rev. Lett.*, **92**, 077205 (2004).
5) G. S. D. Beach, M. Tsoi, and J. L. Erskine, *J. Magn. Magn. Mater.*, **320**, 1272 (2008).
6) K.-J. Kim, R. Hiramatsu, T. Koyama, K. Ueda, Y. Yoshimura, D. Chiba, K. Kobayashi, Y. Nakatani, S. Fukami, M. Yamanouchi, H. Ohno, H. Kohno, G. Tatara, and T. Ono, *Nat. Commun.*, **4**, 2011 (2013).
7) Y. M. Hung, T. Li, R. Hisatomi, Y. Shiota, T. Moriyama, and T. Ono, *J. Magn. Soc. Jpn,* **45**, 6 (2021).
8) Y. M. Hung, Y. Shiota, R. Hisatomi, T. Moriyama, and T. Ono, *Appl. Phys. Express*, **14**, 023001 (2021).
9) I. M. Miron, K. Garello, G. Gaudin, P.-J. Zermatten, M. V. Costache, S. Auffret, S. Bandiera, B. Rodmacq, A. Schuhl, and P. Gambardella, *Nature*, **476**, 189 (2011).
10) L. Liu, C.-F. Pai, Y. Li, H. W. Tseng, D. C. Ralph, and R. A. Buhrman, *Science*, **336**, 555 (2012).
11) L. Liu, O. J. Lee, T. J. Gudmundsen, D. C. Ralph, and R. A. Buhrman, *Phys. Rev. Lett.*, **109**, 096602 (2012).
12) B. Jinnai, C. Zhang, A. Kurenkov, M. Bersweiler, H. Sato, S. Fukami, and H. Ohno, *Appl. Phys. Lett.*, **111**, 102402 (2017).
13) V. Ostwal, A. Penumatcha, Y.-M. Hung, A. D. Kent, and J. Appenzeller, *J. Appl. Phys.*, **122**, 213905 (2017).
14) J. C. Slonczewski, *J. Magn. Magn. Mater.*, **159**, L1 (1996).
15) L. Berger, *Phys. Rev. B*, **54**, 9353 (1996).
16) A. Brataas, A. D. Kent, and H. Ohno, *Nat. Mater.*, **11**, 372 (2012).
17) Y. -H. Wang, S. -H. Huang, D. -Y. Wang, K. -H. Shen, C. -W. Chien, K. -M. Kuo, S. -Y. Yang, and D. -L. Deng, Abstract 2012 *International Electron Devices Meeting*, 29.2.1.
18) M. Lavanant, P. Vallobra, S. P. Watelot, V. Lomakin, A.D. Kent, J. Sun, and S. Mangin, *Phys. Rev. Appl.*, **11**, 034058 (2019).
19) C. Stoner, *Proc. R. Soc. Lond. A*, **165**, 372 (1938).
20) S. Ferrer, J. Álvarez, E. Lundgren, X. Torrelles, P. Fajardo, and F. Boscherini, *Phys. Rev. B*, **56**, 9848 (1997).
21) A. Meo, P. Chureemart, S. Wang, R. Chepulskyy, D. Apalkov, R. W. Chantrell, and R. F. L. Evans, *Sci. Rep.*, **7**, 16729 (2017).
22) K. Garello, I. M. Miron, C. O. Avci, F. Freimuth, Y. Mokrousov, S. Blügel, S. Auffret, O. Boulle, G. Gaudin, and P. Gambardella, *Nat. Nanotechnol.*, **8**, 587 (2013).

Received Aug. 08, 2024; Accepted Sep. 11, 2024

J. Magn. Soc. Jpn., **48**, 116-123 (2024) <Paper>

Dependence of complex magnetic susceptibility on alignment of easy axis in magnetic nanoparticles

Menghao Li[1], Suko Bagus Trisnanto[1], Satoshi Ota[2], Yasushi Takemura[1]
[1]Department of Electrical and Computer Engineering, Yokohama National University, *Yokohama 240-8501, Japan*
[2]Department of Electrical and Electronic Engineering, Shizuoka University, *Hamamatsu 432-8561, Japan*

Superparamagnetic nanoparticles have received significant attention with regard to medical applications of magnetic hyperthermia and magnetic nanoparticle imaging. For magnetic nanoparticles with uniaxial anisotropy, the coexistence of interwell and intrawell modes delays the magnetization response to the applied magnetic field. Therefore, an investigation of these two modes is essential for the study of magnetic moment dynamics. This study focuses on the frequency dependence of AC susceptibility to differentiate samples with varying degrees of easy axis alignment. The results indicate that the alignment of the easy axis separated the two modes of susceptibility. The variation in the activation energy depending on the degree of the easy axis alignment is also discussed, which clarifies the magnetization dynamics and Néel relaxation time of the magnetic nanoparticles.

Keywords: magnetic nanoparticles, superparamagnetism, AC magnetic susceptibility, easy axis of magnetization, magnetization dynamics, activation energy, Néel relaxation.

1. Introduction

Iron oxide nanoparticles with diameters less than 10-20 nm have single magnetic domain structures. They exhibit superparamagnetism owing to their randomized magnetic moment directions caused by thermal fluctuations[1,2]. The growth of these particles can be controlled through thermal and stoichiometric processes during synthesis, and they can be encapsulated with surfactants after screening the core size. Interactions between individual fine particles typically result in aggregates that can be encapsulated to form complex particle structures, known as multi-core magnetic nanoparticles. Although the aggregation of small-core particles increases the hydrodynamic volume, the superparamagnetism of each core ensures the superparamagnetic behavior of multi-core nanoparticles[3-5]. The degree of aggregation of the core particles affects their magnetic response to externally applied magnetic fields[6]. These multi-core magnetic nanoparticles have potential biomedical applications such as in magnetic hyperthermia and magnetic particle imaging[7-9].

A thorough understanding of the magnetization dynamics of magnetic nanoparticles is essential to enhance their performance in medical applications. The easy axes of magnetic anisotropy in magnetic nanoparticles in colloids oscillate in response to an externally applied magnetic field, with the magnetic moments of the particles momentarily deviating from the easy axes and returning to balance at the lowest-energy position. Thermal fluctuation leads to Brownian and Néel relaxation independently in this process, which complicates the analysis of the magnetization dynamics of magnetic particles[10].

The easy axes can be determined by separately analyzing the magnetic moment dynamics [11,12]. The energy barrier results in two modes that describe the relaxation of the magnetic moments along the easy axis of anisotropy, where the interwell relaxation corresponds to magnetization reversal, and the intrawell mode involves the precession of the magnetic moment before stabilization along the easy axis[13]. The average of all the orientations with random easy axes in the colloidal samples can be derived. However, for immobile magnetic particles fixed in a solid material, in which the easy axes of the particles are aligned by applying a DC magnetic field during sample preparation, the anisotropy of the particles results in different magnetic responses depending on the direction of the sample and the applied magnetic field. The two relaxation modes, the interwell and intrawell modes can be distinguished based on the angle between the direction of the easy axis and the detection signal[14,15]. The purpose of this study was to clarify the variations in the activation energies of magnetic nanoparticles with immobile easy axes with different degrees of alignment. We measured the AC susceptibility of samples with random and aligned easy axes and quantified the differences in the magnetization properties depending on the degree of easy axis alignment.

2. Theory

The anisotropy energy E_a of magnetic nanoparticles with uniaxial anisotropy, without considering interactions, is described by

$$E_\mathrm{a} = K_\mathrm{u} V \sin^2\theta, \qquad (1)$$

where K_u is the uniaxial anisotropy constant, V is the volume of the particle, and θ is the angle between the

---

Corresponding author:
Y. Takemura (e-mail: takemura-yasushi-nx@ynu.ac.jp).

easy axis of magnetization and the magnetic moment, respectively.

In a field-free environment, the magnetization of the nanoparticle aligns along the direction of the lowest energy. Thus, the magnetic moment tends to lie in the direction of the anisotropy axis. When an external magnetic field is applied, the easy axis of magnetization and the magnetic moment rotate in response to the external field. The magnetization process of particles with uniaxial anisotropy is typically described by the Stoner-Wohlfarth model, which depicts this process as a balance between the Zeeman energy and anisotropy energy[16]:

$$E = K_\mathrm{u} V \sin^2\theta - m H_\mathrm{eff} \cos(\varphi - \theta), \tag{2}$$

where m, H_eff, and φ denote the moment of the particle, the intensity of the effective field, and the angle between the easy axis and the direction of H_eff, respectively. The effective field $H_\mathrm{eff} = H_\mathrm{dip} + H_\mathrm{app}$ comprises the dipole field H_dip and the applied magnetic field H_app.

The magnetization process of nanoparticles exhibiting superparamagnetism is described by the Langevin function,

$$L(\xi) = \coth(\xi) - \frac{1}{\xi}. \tag{3}$$

Here, ξ is defined as $\xi = \mu_0 m H / k_\mathrm{B} T$, where μ_0, k_B, and T are the magnetic permeability of vacuum, Boltzmann constant, and absolute temperature, respectively.

The rotation of the easy axis is influenced by thermal fluctuations, causing the easy axis to take a certain amount of time–the Brownian relaxation time–to reach the equilibrium position. This time depends on the viscosity of the ambient medium in which the particles are dispersed. Similarly, the rotation of the magnetic moment reaches equilibrium within the Néel relaxation time[17,18]. The ratio of the anisotropy energy to the thermal energy $\sigma = K_\mathrm{u} V / k_\mathrm{B} T$ directly affects the Néel relaxation time τ_N; thus the large volume and anisotropy lead to a transition to the ferromagnetic state. The magnetization of immobile nanoparticles in a solid sample is dominated only by the rotation of the magnetic moments, for which the Brownian eigenfunction can be used to estimate the Néel relaxation time[19]:

$$\tau_\mathrm{N} = \begin{cases} \dfrac{\tau_0 \sqrt{\pi}}{2\sqrt{\sigma}} \exp(\sigma), & \sigma \geq 1 \\ \tau_0 \sigma \left(1 - \dfrac{2}{5}\sigma + \dfrac{48}{875}\sigma^2\right)^{-1}, & \sigma \ll 1 \end{cases} \tag{4}$$

where τ_0 corresponds to the precession of the magnetic moment and can be estimated with the ferromagnetic resonance[20]. τ_0 is of the order of 10^{-9} to 10^{-11} s. The magnetic moment rotation resonates at the Néel relaxation frequency $f_\mathrm{N} = (2\pi\tau_\mathrm{N})^{-1}$. When an AC magnetic field is applied to a magnetic nanoparticle, its magnetic moment oscillates in response. This oscillation gradually fails to follow the change in the magnetic field, with the phase difference between the magnetic field and magnetization increasing with an increase of the AC field frequency until reaching a maximum at $f = f_\mathrm{N}$. The reduction in the oscillation amplitude of the magnetic moment results in a continuous decrease in magnetization during this process. The Debye model generally describes the susceptibility spectra with relaxation type[21]

$$\chi(\omega) = \frac{\chi_0}{1 + i\omega\tau}. \tag{5}$$

Here, $\tau = \tau_\mathrm{N}$ is the relaxation time, ω is the angular frequency of the AC magnetic field, and χ_0 is the susceptibility under an applied magnetic field of low intensity.

The real part χ' and imaginary part χ'' of the susceptibility correspond to the component of the magnetization oscillating with the AC magnetic field and the phase delay between the magnetization and AC magnetic field, respectively. They are described as

$$\chi'(\omega) = \frac{\chi_0}{1 + (\omega\tau_\mathrm{N})^2}, \tag{6}$$

$$\chi''(\omega) = \frac{\chi_0(\omega\tau_\mathrm{N})}{1 + (\omega\tau_\mathrm{N})^2}. \tag{7}$$

Depending on the directions of the easy axis of the magnetic anisotropy and the AC magnetic field, susceptibility χ can be further divided into longitudinal and transverse susceptibility. For a sample with a random orientation of the easy axis, the two components define χ with a relationship[22]:

$$\chi(\omega) = \frac{1}{3}\left(\chi_\parallel(\omega) + 2\chi_\perp(\omega)\right). \tag{8}$$

While the longitudinal component $\chi_\parallel$ corresponds to the reversal of the magnetization due to thermal fluctuations, the transverse component $\chi_\perp$ corresponds to the alignment of moment along the internal effective field H_eff with precession. The magnetization dynamics can be described using the Landau–Lifshitz–Gilbert (LLG) equation[23]:

$$\frac{dM}{dt} = -\gamma M \times H_\mathrm{eff} + \frac{\alpha}{M_s} M \times \frac{dM}{dt}, \tag{9}$$

which includes gyromagnetic ratio γ, saturation magnetization M_s and damping factor α. The characteristics of the transverse component depend on α and evolve from a relaxation type to a resonance type with small α. A low energy barrier σ results in a distribution of precession rate and also changes the susceptibility spectra. By substituting the Debye equation into the longitudinal component of Eq. 8, the following equation is obtained:

$$\chi(\omega)=\frac{1}{3}\left(\frac{\chi_\parallel}{1+i\omega\tau_\parallel}+2\chi_\perp\right). \tag{10}$$

When the frequency of the AC magnetic field is lower than the precession frequency, the frequency dependence of the susceptibility is dominated by the longitudinal component.

3. Experiments

3.1 Measurement method

The AC susceptibilities of the nanoparticle samples were measured using a frequency response analyzer (FRA51615, NF Corporation, Japan). The frequency range was from 100 Hz to 10 MHz. A detection coil was used to detect magnetization changes in the samples[24]. An AC magnetic field H_{ac} with a magnitude of H_{ac} = 0.1 mT/μ_0 was applied to the samples.

The induced voltage V_0 in the detection coil without an inserted sample is described as

$$V_0(t)=NS\omega\mu_0H_0\sin\omega t, \tag{11}$$

where H_0, N, and S are the applied AC magnetic field intensity, number of turns, and cross-sectional area of the detection coil, respectively. The induced voltage V_s was measured when the sample was inserted into the detection coil. V_s is described using the relative permeability μ_r of the sample and a phase delay β,

$$V_s(t)=NS\omega\mu_r\mu_0H_0\sin(\omega t-\beta). \tag{12}$$

The complex magnetic permeability μ_{rc} can be described by μ_{rc0} and β as follows:

$$\mu_{rc}=\mu_{rc0}(\cos\beta-i\sin\beta). \tag{13}$$

The complex magnetic susceptibility can be described by

$$\chi=\chi'-i\chi''=\mu_{rc}-1. \tag{14}$$

Thus, its real and the imaginary parts can be described as

$$\chi'=\mu_{rc0}\cos\beta-1, \tag{15}$$

$$\chi''=\mu_{rc0}sin\beta, \tag{16}$$

respectively[24], and the absolute value of χ is described as

$$|\chi|=\sqrt{\chi'^2+\chi''^2}. \tag{17}$$

In this study, the induced voltage and phase delay were measured before and after inserting the samples, and the susceptibility spectra were obtained using the equations above.

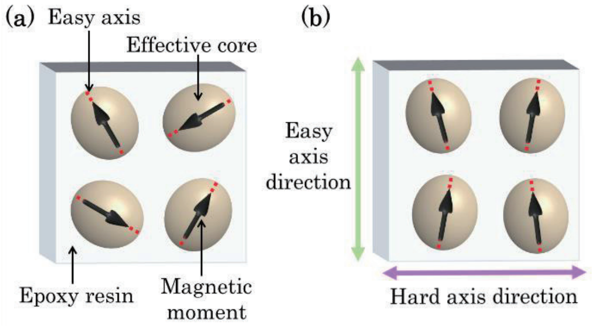

Fig. 1 Schematics of solid-state samples containing magnetic nanoparticles. (a) Random sample with random directions of easy axis of magnetic anisotropy. (b) Aligned sample with aligned orientation of easy axis, which can be measured along the easy and hard axis directions.

Static magnetization characteristics were measured using a vibrating sample magnetometer (VSM, Toei Industry Co., Ltd., Japan) at room temperature. The maximum intensity of the applied magnetic field was 5 mT/μ_0 or 1500 mT/μ_0.

3.2 Samples

Ferucarbotran (Meito Sangyo Co. Ltd., Japan) is the raw material for Resovist®, which contains carboxy dextran coated multi-core maghemite (γ-Fe_2O_3) and magnetite (Fe_3O_4) nanoparticles with a broadening magnetic moment distribution[25]. Ferucarbotran was mixed with epoxy resin and stirred to prepare solid-state samples containing immobile magnetic nanoparticles. In these solid samples, the easy axes of magnetic anisotropy are fixed, as shown in Fig. 1. “The random samples” were prepared as a result of solidification for eight hours after mixing in epoxy resin without applying any magnetic field. The iron weight density of these random samples was either 46 or 10 mg_{Fe}/mL.

When a static magnetic field was applied to the sample during solidification, “the aligned samples” with an aligned orientation of the easy axes were obtained. The iron weight density of samples A1 and A2 was 46 mg_{Fe}/mL, which were solidified in an applied magnetic field of 0.8 T/μ_0 and 1 T/μ_0, respectively. The iron weight density of sample A3 was 10 mg_{Fe}/mL, which was also solidified in an applied magnetic field of 0.8 T/μ_0. For the samples A1, A2, and A3, the magnetization properties both parallel and perpendicular to the aligned easy axis orientation could be measured, which were denoted as “easy axis direction” and “hard axis direction,” respectively as shown in Fig. 1. The sample specifications are summarized in Table 1. In this study, we assumed that the anisotropy of the particles in the samples was uniaxial[26].

4. Results and discussion

4.1 Static magnetization characteristics

The static magnetization characteristics of the samples,

Table 1 Equivalent iron concentration and applied magnetic field intensity during solidification of aligned samples: A1, A2, and A3 and random samples: R1 and R2.

Samples	A1	A2	A3	R1	R2
Equivalent iron concentration ($\mathrm{mg_{Fe}/mL}$)	46	46	10	46	10
Magnetic field intensity for alignment (T/μ_0)	0.8	1.0	0.8	—	—

normalized by the saturation magnetization, are shown in Fig. 2(a). The saturation magnetization was calculated from the major magnetization curves measured under an applied magnetic field up to 1500 mT/μ_0 by fitting the Langevin function. Figure 2(a) shows the magnetization curves of the aligned samples A1, A2, and A3 measured along their easy and hard axes. The figure also shows the magnetization curves of random samples R1 and R2 to compare the magnetization properties between random and aligned easy-axis samples with the same iron concentration.

Random samples R1 and R2 exhibited superparamagnetic features with no coercivity. The magnetizations along the easy axes of A1, A2, and A3 were greater than those of the random samples. The magnetizations of the samples with uniaxial anisotropy tended to align along the easy axis of magnetization. The magnetizations along the hard axis were smaller than those of random samples.

Figure 2(b) shows the minor magnetization curves of A1, A2, and A3 measured under an applied magnetic field up to 5 mT/μ_0. The aligned samples exhibit coercivity along the easy axis direction, as shown in Figs 2(a) and 2(b), which are attributed to the stable magnetic moment along the easy axes of the magnetization anisotropy[6),25)]. The increasing degree of the easy-axis orientation increased the dipole field from neighboring particles, thereby enhancing the contribution of the magnetization anisotropy of the samples[27)]. The magnetic moment overcomes the anisotropy energy and flips perpendicularly to the easy axis of the particles, resulting in a lower magnetization along the hard axis direction of the aligned samples than that of the random samples.

We quantified the degree of easy axis alignment[28)] by using the following equation:

$$R_{\mathrm{M}} = \frac{M_{\mathrm{ani}}}{M_{\mathrm{ran}}}. \tag{18}$$

Here, M_{ani} denotes the difference of the magnetizations along the easy and hard axes directions of the aligned sample, and M_{ran} is the magnetization of the random sample with the same iron concentration. We used the magnetization values at the applied field intensity at 5 mT/μ_0 of the major magnetization curves shown in Fig. 2(a) for M_{ani} and M_{ran}.

Figure 3 shows the difference between the energy ΔE_{a} along the easy and hard axes directions of the aligned sample as a function of the degree of easy axis alignment,

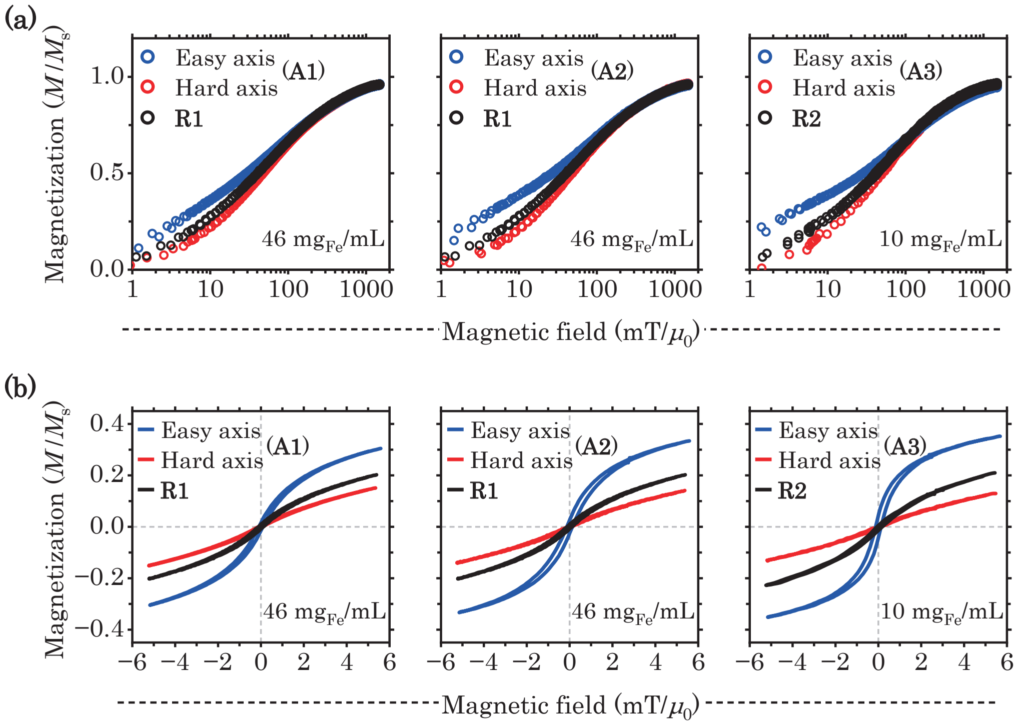

Fig. 2 (a) Major and (b) minor magnetization curves of static magnetization properties of the samples. The maximum intensities of the applied magnetic field were 1500 mT/μ_0 and 5 mT/μ_0, respectively.

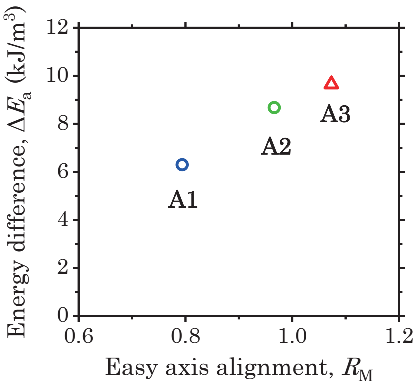

Fig. 3 Difference between the energy ΔE_{a} along the easy and hard axis directions of the aligned sample as a function of the degree of easy axis alignment R_{M}.

ΔE_{a} is calculated from the major magnetization curves using the following equation:

$$\Delta E_{\mathrm{a}} = \mu_0 \int (M_{\mathrm{easy}} - M_{\mathrm{hard}}) dH_{\mathrm{app}}, \tag{19}$$

where M_{easy} and M_{hard}, are the magnetization along the easy- and hard-axis directions, respectively, and H_{app} is the applied magnetic field intensity. A monotonic dependence of ΔE_{a} on R_{M} is observed as shown in Fig. 3.

R_{M} of A3 with the lower iron concentration was greater than that of A1 and A2. This was because of the reduced dipole interaction between the magnetic nanoparticles in the sample with a lower iron concentration, allowing the particles to rotate more and align in the direction of the applied magnetic field. R_{M} of A2 was greater than that of A1, which was attributed to a larger applied field intensity during the solidification of A2.

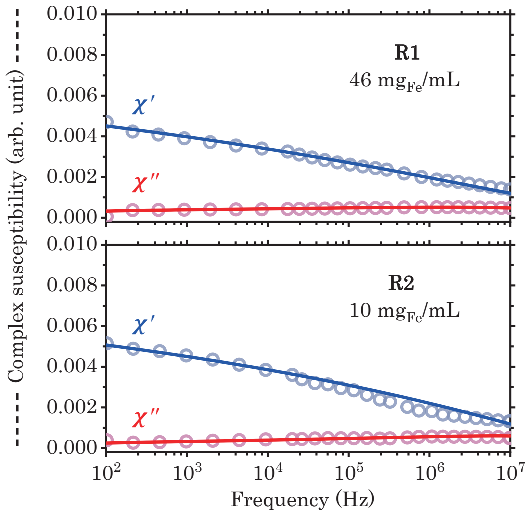

Fig. 4 Frequency-dependent complex susceptibility of the random samples; the measurement data (open circles) and fitted lines were obtained using Eqs. (21) and (22) (solid lines).

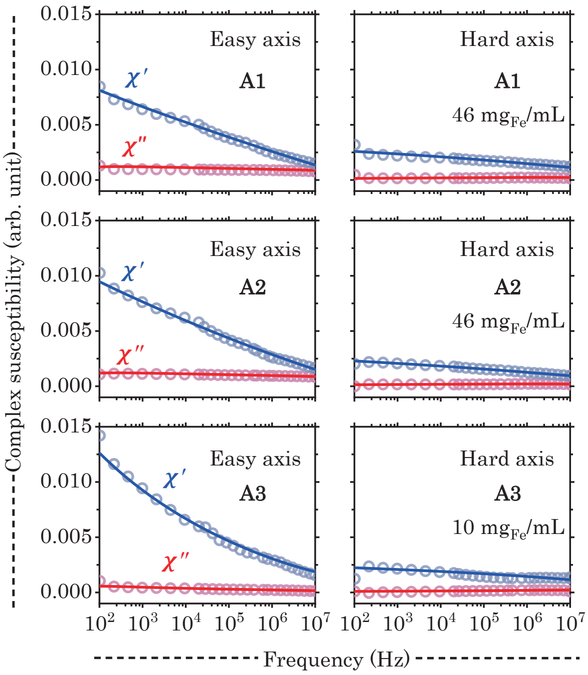

Fig. 5 Frequency dependence of the complex susceptibility of the aligned samples; the measurement data (open circles) and fitted lines were obtained using Eqs. (21) and (22) (solid lines).

4.2 AC susceptibility of random samples

The complex AC susceptibility spectra measured using random samples are shown in Fig. 4. Because the measured samples consisted of the same magnetic nanoparticles, the susceptibility was normalized by the iron weights of the samples. Typical characteristics of Debye relaxation were not observed in the measured frequency range up to 10 MHz. However, the real parts of the AC susceptibility originating from the magnetization component oscillating with the applied alternating magnetic field decreased. The nonzero values of the imaginary part suggest a phase delay in the magnetization rotation with respect to the applied magnetic field. This behavior was attributed to the Néel relaxation of the effective magnetic moments with a wide distribution of activation energies in the samples. The susceptibility spectra were fitted using a log-normal distribution of the activation energy ratios σ[6]:

$$\rho(\sigma) = \frac{1}{\sqrt{2\pi} a\sigma} \exp\left(-\frac{1}{2}\left(\frac{\ln(\sigma) - b}{a}\right)^2\right), \tag{20}$$

where a and b denote standard deviation and mean, respectively. The Néel relaxation time τ_{N} is calculated by Eq. (4). Eqs. (6) and (7) can be derived as

$$\chi'(\omega) = \int \frac{\chi_0 \rho(\tau_{\mathrm{N}})}{1 + (\omega\tau_{\mathrm{N}})^2} + \chi_\infty d\tau_{\mathrm{N}}, \tag{21}$$

$$\chi''(\omega) = \int \frac{\chi_0 \rho(\tau_N)\omega\tau_N}{1+(\omega\tau_N)^2} d\tau_N. \qquad (22)$$

Here, χ_∞ is the susceptibility at a sufficiently high frequency, which can be approximated as zero. The weighted averages of activation energy ratios $\bar{\sigma}$ of the samples R1 of 46 $\mathrm{mg_{Fe}}$/mL and R2 of 10 $\mathrm{mg_{Fe}}$/mL in the measured frequency region were 7.86 and 8.21, respectively, which were consistent with a previous analysis based on the effective core model in an almost field-free environment[6].

4.3 AC susceptibility of aligned samples

The real and imaginary components of the AC susceptibility for aligned samples A1, A2, and A3 are shown in Fig. 5. Similar to random samples, no apparent peaks appeared in the imaginary components. Because of the tendency of the magnetic moments to align along the easy axis, the magnetization along the easy axis was evidently greater than that along the hard axis. The real parts decrease to small values in the high-frequency region, indicating that a significant proportion of the magnetic moments are effectively unable to rotate during the observation time. Consequently, the longitudinal components were small in the high-frequency region, whereas the transverse components remained large. In contrast, the apparent magnetic susceptibility in the hard-axis direction was mainly dominated by the transverse component[15]. Because the precession of magnetic moments typically occurs in the GHz range, the imaginary components indicating the phase delay of the magnetic moment rotation in the frequency range of this experiment are negligible[29,30]. The decrease in the real parts also suggests a distribution in the easy-axis direction[32].

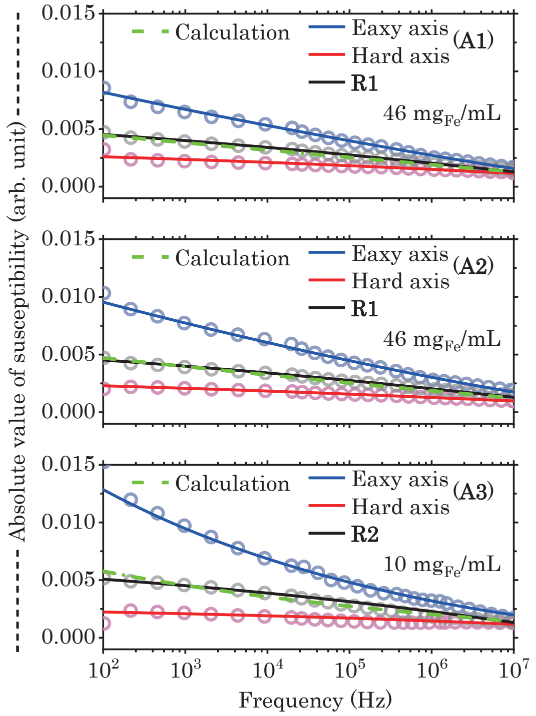

Fig. 6 Absolute values of susceptibility; the measurement data (open circles) and fitted lines were obtained by using Eqs. (21) and (22) (solid lines), and calculated values were obtained using Eq. (8) (dashed lines).

Among samples A1 and A2, which contain the same iron concentration, A2—with a larger degree of easy axis alignment—exhibited a slightly larger real part of the susceptibility in the easy axis direction than A1 in the low-frequency region. Consequently, the longitudinal component of the susceptibility of A2 in the hard-axis direction was smaller than that of A1, which can be observed as a slight difference in the imaginary components of these samples.

4.4 Activation energy depending on easy axis alignment

The frequency-dependent susceptibility spectra indicate the transition of the effective dynamics of the magnetic moments from longitudinal to transverse modes. Figure 6 shows the absolute values of the susceptibilities of aligned samples A1, A2, and A3. We estimated the susceptibilities with random orientations of the easy axis from the measured results of the aligned samples using Eq. (8), as indicated by the green dotted lines in the figure. These calculated values agree with the measured susceptibilities of the random samples.

Sample A3, with a higher degree of easy axis alignment, exhibited larger magnetization along the easy axis direction, as shown in Fig. 5, owing to the smaller angular distribution of the easy axes. This resulted in a larger susceptibility along the easy-axis direction and a rapid decrease in its frequency-dependent spectra, as shown in Fig. 6, indicating more longitudinal modes in the easy-axis direction. In contrast, the susceptibility along the hard axis direction reflects a transverse mode that remains extremely small and constant.

In this study, we define the difference in the susceptibilities, $\Delta\chi = \chi_{\max} - \chi_{\min}$ to evaluate the degree of alignment of the easy axis, where $\chi_{\max}$ and $\chi_{\min}$ denote the absolute values of susceptibilities at 100 Hz

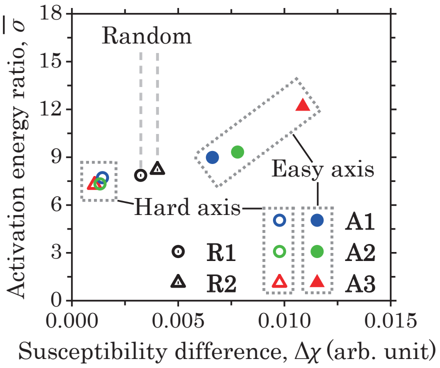

Fig. 7 Relationship between the weighted average of the activation energy ratio $\bar{\sigma}$ and the susceptibility difference $\Delta\chi$.

and 10 MHz. Figure 7 shows the dependence of the weighted average of activation energy ratios $\bar{\sigma}$ on $\Delta\chi$. $\Delta\chi$ calculated from the susceptibilities along the easy axis was higher than that along the hard axis. The activation energy ratios $\bar{\sigma}$ of all the samples were significantly larger than 1 due to intrinsic dipole interaction[6], which indicates that the anisotropy energy is considerably larger than the thermal energy. Thus, the effect of thermal fluctuations is negligible when estimating the energy difference in section 4.1. The activation energy ratios $\bar{\sigma}$ were proportional to $\Delta\chi$. The average activation energy ratios $\bar{\sigma}$ and the difference in the magnetic susceptibility $\Delta\chi$ were derived from the same fitting results of the experimental data, which indicate the degree of alignment and show a consistency. $\bar{\sigma}$ along the easy axis was greater than that along the hard axis, and $\bar{\sigma}$ for the random samples was intermediate to those along the easy and hard axes of the aligned samples. This is because the magnetic moments overcome the anisotropy energy of the easy axis using thermal energy to rotate in response to an applied magnetic field. As for the easy axis, $\bar{\sigma}$ increased with increasing $\Delta\chi$ for the aligned samples of A1, A2, and A3.

This originates from the smaller angle distribution of the aligned easy axis and indicates that the susceptibility is predominantly determined by the thermal relaxation of the magnetization rotation. Moreover, the anisotropy energy dominates the activation energy ratios $\bar{\sigma}$ in the applied magnetic field of 0.1 mT, wherein the contribution of the Zeeman energy is negligible. For the samples measured in this experiment, the dipole field H_{dip} from the neighboring particles was not negligible. The increasing degree of alignment of the easy axis increased the contribution of H_{dip} from neighboring particles, enhanced the anisotropy, and resulted in a large $\bar{\sigma}$. In contrast, the magnetic moments rotated by a small angle in response to the magnetic field applied in the hard axis direction of the aligned samples. $\bar{\sigma}$ was small because it was not affected by the anisotropy energy. Owing to the small angle between the directions of the hard axis and the applied AC magnetic field, the longitudinal component of susceptibility was small. As indicated by Eq. (4), the Néel relaxation time depends on activation energy. These measurement results agree with the analysis of the differences in Néel relaxation times depending on the easy axis alignment[31].

5. Summary

The complex susceptibilities of magnetic nanoparticles exhibiting superparamagnetic features were studied. We measured the magnetization properties of solid-state samples containing magnetic nanoparticles with random and aligned easy magnetization axes. The results verified the differences in susceptibility between the aligned and randomly oriented samples, supporting a model that separates the longitudinal and transverse modes of susceptibility. In our study, because of the alignment distribution of the easy axis of magnetization, both modes were observable in both directions of the sample. However, as the degree of alignment of the easy axes increased, the separation between the longitudinal and transverse susceptibility modes became more apparent.

Acknowledgements This study was partially supported by JSPS KAKENHI JP20H05652, JP20H02163, and JP22K14268.

References

1) R. H. Kodama: *J. Magn. Magn. Mater.*, **200**, 359 (1999).
2) C. P. Bean and J. D. Livingston: *J. Appl. Phys.*, **30**, S120 (1959).
3) A. G. Roca, L. Gutiérrez, H. Gavilán, M. E. Fortes Brollo, S. Veintemillas-Verdaguer, and M. del Puerto Morales: *Adv. Drug Deliver. Rev.*, **138**, 68 (2019).
4) L. Gutiérrez, R. Costo, C. Grüttner, F. Westphal, N. Gehrke, D. Heinke, A. Fornara, Q. A. Pankhurst, C. Johansson, S. Veintemillas-Verdaguer, and M. P. Morales: *Dalton Trans.*, **44**, 2943 (2015).
5) F. Ahrentorp, A. Astalan, J. Blomgren, C. Jonasson, E. Wetterskog, P. Svedlindh, A. Lak, F. Ludwig, L. J. van IJzendoorn, F. Westphal, C. Grüttner, N. Gehrke, S. Gustafsson, E. Olsson, and C. Johansson: *J. Magn. Magn. Mater.*, **380**, 221 (2015).
6) S. B. Trisnanto and Y. Takemura: *J. Appl. Phys.*, **130**, 064302 (2021).
7) D. Eberbeck, C. L. Dennis, N. F. Huls, K. L. Krycka, C. Grüttner, and F. Westphal: *IEEE Trans. Magn.*, **49**, 269 (2013).
8) H. Kratz, M. Taupitz, A. Ariza de Schellenberger, O. Kosch, D. Eberbeck, S. Wagner, L. Trahms, B. Hamm, and J. Schnorr: *PLoS One*, **13**, 1 (2018).
9) C. Blanco-Andujar, D. Ortega, P. Southern, Q. A. Pankhurst, and N. T. K. Thanh: *Nanoscale*, **7**, 1768 (2015).
10) S. B. Trisnanto, S. Ota, and Y. Takemura: *Appl. Phys. Express.*, **11**, 075001 (2018).
11) K. Enpuku, A. L. Elrefai, J. Gotou, S. Yamamura, T. Sasayama, and T. Yoshida: *J. Appl. Phys.*, **130**, 113903 (2021).
12) T. Q. Bui, A. J. Biacchi, C. L. Dennis, W. L. Tew, A. R. Hight Walker, and S. L. Woods: *Appl. Phys. Lett.*, **120**, 012407 (2022).
13) Y. L. Raikher and V. I. Stepanov: *Microelectron. Eng.*, **69**, 317 (2003).
14) G. Shi, R. Takeda, S. B. Trisnanto, T. Yamada, S. Ota, and Y. Takemura: *J. Magn. Magn. Mater.*, **473**, 148 (2019).
15) F. Ludwig, C. Balceris, C. Johansson, and C. Johansson: *IEEE Trans. Magn.*, **53,** 11 (2017).
16) E. C. Stoner and E. P. Wohlfarth: *Phil. Trans. R. Soc. Lond* A, **240**, 599 (1948).
17) J. Dieckhoff, D. Eberbeck, M. Schiling, and F. Ludwig: *J. Appl. Phys.*, **119**, 043903 (2016).
18) W. F. Brown: *Phys. Rev.*, **130**, 1677 (1963).
19) P. C. Fannin and S. W. Charles: *J. Phy. D: Appl. Phys.*, **27**, 185 (1994).
20) P. C. Fannin: *J. Mol. Liq.*, **114**, 79 (2004).
21) W. T. Coffey, P. J. Cregg, and Y. U. P. Kalmykov: *Adv. Chem. Phys.*, (John Wiley & Sons, Inc., 2007), pp. 263–464.
22) M. I. Shliomis and V. I. Stepanov: *J. Magn. Magn. Mater.*, **122**, 176, (1993).
23) T. L. Gilbert: *IEEE Trans. Magn.*, **40**, 3443 (2004).
24) S. Noguchi, S. B. Trisnanto, T. Yamada, S. Ota, and Y. Takemura: *J. Magn. Soc. Jpn.*, **46**, 42 (2022).
25) T. Yoshida, N. B. Othman, and K. Enpuku: *J. Appl. Phys.*, **114**, 173908 (2013).
26) K. Enpuku, A. L. Elrefai, T. Yoshida, T. Kahmann, J. Zong, T. Viereck, and F. Ludwig: *J. Appl. Phys.*, **127**, 133903 (2020).
27) E. Sasaoka, C. Yang, S. B. Trisnanto, Z. Song, S. Ota, and Y. Takemura: *J. Magn. Soc. Jpn.*, **47**, 115 (2023).
28) A. L. Elrefai, T. Sasayama, T. Yoshida, and K. Enpuku:

IEEE Trans. Magn., **57**, 1 (2021).
29) Y. Pu, L. Tonthat, T. Murayama, K. Okita, and S, Yabukami: *AIP Adv.*, **13**, 025129 (2023).
30) J. Dubreuil and J. S. Bobowski: *J. Magn. Magn. Mater.*, **489**, 165387 (2019).
31) T. Yoshida, Y. Matsugi, N. Tsujimura, T. Sasayama, K. Enpuku, T. Viereck, M. Schilling, and F. Ludwig: *J. Magn. Magn. Mater.*, **427**, 162 (2017).

Received Aug. 08, 2024; Revised Aug. 29, 2024; Accepted Sep. 06, 2024

Editorial Committee Members・Paper Committee Members

S. Yabukami and T. Taniyama (Chairperson), N. H. Pham, D. Oyama and M. Ohtake (Secretary)
H. Aoki M. Goto T. Goto K. Hioki S. Inui K. Ito
M. Iwai Y. Kamihara H. Kikuchi T. Kojima H. Kura A. Kuwahata
K. Masuda Y. Nakamura K. Nishijima T. Nozaki T. Sato E. Shikoh
T. Suetsuna K. Suzuki Y. Takamura K. Tham T. Tanaka M. Toko
N. Wakiya S. Yakata A. Yao S. Yamada M. Yoshida

N. Adachi K. Bessho M. Doi T. Doi T. Hasegawa R. Hashimoto
S. Haku S. Honda S. Isogami T. Kawaguchi T. Kawai N. Kikuchi
K. Kobayashi T. Maki S. Muroga M. Naoe T. Narita M. Sakakibara
Y. Sato S. Seino M. Sekino Y. Shiota T. Shirokura S. Sugahara
I. Tagawa K. Tajima M. Takezawa T. Takura S. Tamaru T. Yamazaki
T. Yoshida S. Yoshimura

Notice for Photocopying

If you wish to photocopy any work of this publication, you have to get permission from the following organization to which licensing of copyright clearance is delegated by the copyright owner.

〈All users except those in USA〉
Japan Academic Association for Copyright Clearance, Inc. (JAACC)
6–41 Akasaka 9-chome, Minato-ku, Tokyo 107–0052 Japan
Phone 81–3–3475–5618 FAX 81–3–3475–5619 E-mail: info@jaacc.jp

〈Users in USA〉
Copyright Clearance Center, Inc.
222 Rosewood Drive, Danvers, MA01923 USA
Phone 1–978–750–8400 FAX 1–978–646–8600

If CC BY 4.0 license icon is indicated in the paper, the Magnetics Society of Japan allows anyone to reuse the papers published under the Creative Commons Attribution International License (CC BY 4.0).
Link to the Creative Commons license: http://creativecommons.org/licenses/by/4.0/
Legal codes of CC BY 4.0: http://creativecommons.org/licenses/by/4.0/legalcode

編集委員・論文委員

藪上　信（理事）　谷山智康（理事）　Pham NamHai（幹事）　大竹　充（幹事）　小山大介（幹事）
青木英恵　伊藤啓太　乾　成里　岩井守生　神原陽一　菊池弘昭　藏　裕彰　桑波田晃弘　小嶋隆幸
後藤太一　後藤　穣　佐藤　拓　仕幸英治　末綱倫浩　鈴木和也　高村陽太　田中哲郎　都甲　大
Kim Kong Tham　仲村泰明　西島健一　野崎友大　日置敬子　増田啓介　八尾　惇　家形　諭
山田晋也　吉田征弘　脇谷尚樹

安達信泰　磯上慎二　川井哲郎　川口昂彦　菊池伸明　小林宏一郎　榊原　満　佐藤佑樹　塩田陽一
白倉孝典　菅原　聡　清野智史　関野正樹　田倉哲也　田河育也　竹澤昌晃　田島克文　田丸慎吾
土井達也　土井正晶　直江正幸　成田正敬　白　怜士　橋本良介　長谷川　崇　別所和宏　本多周太
槙　智仁　室賀　翔　山崎貴大　吉田　敬　吉村　哲

複写をされる方へ

当学会は下記協会に複写複製および転載複製に係る権利委託をしています．当該利用をご希望の方は，学術著作権協会（https://www.jaacc.org/）が提供している複製利用許諾システムもしくは転載許諾システムを通じて申請ください．

権利委託先：一般社団法人学術著作権協会
〒107–0052 東京都港区赤坂9–6–41　乃木坂ビル
電話（03）3475–5618　FAX（03）3475–5619　E-mail: info@jaacc.jp

ただし，クリエイティブ・コモンズ [表示 4.0 国際] (CC BY 4.0)の表示が付されている論文を，そのライセンス条件の範囲内で再利用する場合には，本学会からの許諾を必要としません．
クリエイティブ・コモンズ・ライセンス http://creativecommons.org/licenses/by/4.0
リーガルコード http://creativecommons.org/licenses/by/4.0/legalcode.ja

---

Journal of the Magnetics Society of Japan

Vol. 48 No. 6 (通巻第336号) 2024年11月1日発行

Vol. 48 No. 6 Published Nov. 1, 2024
by the Magnetics Society of Japan
Tokyo YWCA building Rm207, 1–8–11 Kanda surugadai, Chiyoda-ku, Tokyo 101–0062
Tel. +81–3–5281–0106　Fax. +81–3–5281–0107

Printed by JPC Co., Ltd.
Sports Plaza building 401, 2–4–3, Shinkamata Ota-ku, Tokyo 144–0054
Advertising agency: Kagaku Gijutsu-sha

発行：(公社)日本磁気学会　101–0062　東京都千代田区神田駿河台 1–8–11　東京YWCA会館 207 号室
製作：ジェイピーシー　144–0054　東京都大田区新蒲田 2–4–3　スポーツプラザビル401　Tel.（03）6715–7915
広告取扱い：科学技術社　111–0052　東京都台東区柳橋 2–10–8　武田ビル4F　Tel.（03）5809–1132

Copyright ©2024 by the Magnetics Society of Japan